



Gaseous counters with CsI photocathodes: The COMPASS RICH

S. Dalla Torre

INFN Trieste, Trieste, Italy

ARTICLE INFO

Keywords:

RICH
COMPASS
Gaseous photon detectors
CsI
MWPC
MPGD
MAPMT
fused silica lens telescope
PID

ABSTRACT

COMPASS RICH is a wide acceptance Cherenkov imaging counter with gas radiator, where single photon detection is performed by gaseous detectors and multianode photomultiplier tubes. It accomplishes high-momentum hadron identification in the COMPASS spectrometer at CERN SPS, which is dedicated to hadron physics studies. The counter, designed and built in the last years of the twentieth century, has been in operation since 2001. It has been upgraded several times over the 20 years of operation and, in particular, the photon detection system has been renewed twice, in 2005/06 and in 2015/16, to improve matching the demanding goals of the COMPASS physics programme and the continuously increasing trigger rate.

The RICH has adopted the state-of-the-art technologies enriched with original complements for radiator gas handling, the ultraviolet mirror wall, the multiwire proportional chambers equipped with CsI photocathodes, the multianode photomultiplier tubes coupled to telescopes of fused silica lenses and the read-out electronics. It is the first RICH counter where, in a recent upgrade, part of the original gaseous photon detectors have been replaced with single photon detection by micropattern gaseous detectors, thanks to an original development.

The RICH design principle, construction, upgrades and performance are reported.

1. Introduction

The COMPASS Collaboration is devoted to a wide and diversified programme in hadron physics [1], which includes the study of the spin structure of the nucleons, charm spectroscopy and diffractive processes. More recently, the physics programme has been enlarged so to include the study of the Drell–Yan process on a polarized target and measurements of a delicate exclusive channel, the Deeply Virtual Compton Scattering (DVCS), opening the way to the so-called nucleon tomography. The study of the spin structure of the nucleons is continuing and measurements on a polarized deuterium target are planned in 2021, while a substantial enlargement of the physics reaches is envisaged in the following years as depicted in a recently submitted letter of intent [2]. This rich programme is pursued by Deep Inelastic Scattering (DIS), Semi-Inclusive DIS (SIDIS) and exclusive measurements at high rate and covering a wide phase-space region of the interaction products. The COMPASS spectrometer [3,4] has been designed to match all the requirements dictated by the needs of the physics programme.

The COMPASS spectrometer is sitting on the CERN SPS M2 beam line, providing a high energy polarized muon beam, which is a world-wide unique facility, and high energy secondary hadron beams. The muon beam is accompanied by an intense beam halo, which originates in the long (~600 m) beam section where the pions, generated from the scattering of the SPS p beam off a Be target, decay. The beam transport system collects the muons in the desired momentum range and transport them to the experimental hall. Escaping muons continue

their flight in the beam tunnel or through the ground material around it. A good fraction of them enriches the experimental hall; this halo muons have trajectories roughly parallel to the beam line, even if at large distance from it. Therefore, the beam halo transversally extends over metres and the COMPASS spectrometer detectors have to take into account the related background. Alternatively, the M2 beam line also provides intense hadron beams.

The spectrometer is characterized by a wide angular acceptance obtained with a two-stage strategy, where the first spectrometer is mainly dedicated to large angle acceptance and the second one to precise analysis of the high momentum particles. Both spectrometers are equipped with magnets for particle momentum analysis. The tracking system is organized in telescopes with different angular acceptance and related granularity: the very small angle, the small angle and the large angle telescope. Muon identification is assured by muon filters, while electromagnetic particles are identified with electromagnetic calorimeters. Hadron calorimeters are used for part of the measurements. A COMPASS jewel is the long solid state polarized target, which is an essential ingredient for the spin physics measurements.

The identification of the hadron species is assured by the RICH, designed to match the overall requirements of the COMPASS physics programme and to be harmoniously integrated in the spectrometer. The present article is dedicated to this counter. The main source of information for the present review are Refs. [5–15].

The article is organized as follows. The detector requirements and the design principle are presented in Section 2. The detector evolution

E-mail address: Silvia.DallaTorre@ts.infn.it.

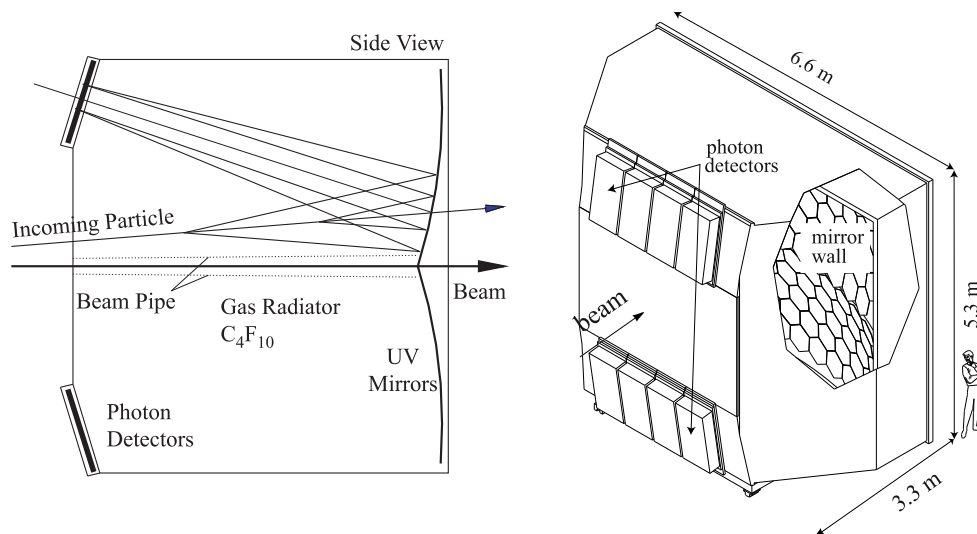


Fig. 1. A scheme of principle (left) and an artist view (right) of the COMPASS RICH-1 detector.

obtained by several upgrade actions is summarized in Section 3. Section 4 is dedicated to the radiator gas and gas system, Section 5 to the mirror system. Section 6 reviews the photon detectors. In particular, the first generation of the gaseous photon detectors is discussed in Section 6.1, the micropattern gaseous photon detectors in Section 6.2, while the usage of multianode photomultiplier tubes is discussed in Section 6.3. Material budget aspects are reported in Section 7. Section 8 is dedicated to hadron Particle IDentification (PID) with the RICH.

2. The design of COMPASS RICH

The detector design is based on the requirements coming from the physics programme, as presented in the COMPASS proposal [16].

Wide angular acceptance is requested in order to match the acceptance of the first stage of the COMPASS spectrometer: 400 mrad in the vertical plane and 500 mrad in the horizontal plane, where the acceptance is increased to account for the trajectory bending by the first spectrometer magnet. Hadron identification at $3\text{-}\sigma$ up to about 50 GeV/c has to be provided in the central region, where the images due to the high momentum hadrons are formed. These demanding requirements come from the charm spectroscopy studies, where positive π and K identification is needed as well as from those nucleon spin-dependent studies by SIDIS measurements based on the identification of the hadrons in the final state. Hadron identification is also a powerful handle in low cross-section processes affected by a large competitive background; a relevant example is provided in Section 8.

The average number of charged particle trajectories reaching the RICH radiator volume is between four and seven, according to the different items of the COMPASS physics programme. The background in the RICH detector is due to two main sources. The most relevant one is related to the muon beam and to its peculiar nature (Section 1). The muons of the beam halo, due to the distribution of their trajectories, are expected to form ring images superimposed to those of the particle scattered at small angle. Of course, the large majority of the images due to Cherenkov photon from halo muons are out of time and not accompanied by reconstructed trajectories. Nevertheless, they are the source of a severe background, that had been already considered in the design phase, even if its rate resulted larger than what predicted by the simulation exercises performed before starting the data taking. This background source is the main motivation of the 2005–2006 upgrade of the photon detector system (Section 3). Another, less severe source of background, are the Bremsstrahlung electrons generated in the material upstream of the RICH, even outside the spectrometer acceptance, as it is the case for the muons of the beam halo crossing the yokes of the first

spectrometer magnet. It was expected that this background source has a very moderate impact on the data resolution, as it could be verified later.

In the COMPASS two-stage spectrometer, the RICH is sitting upstream of the first stage calorimeters and of the second spectrometer stage. Therefore, the overall material budget has to be small and a design reference figure is 20% of radiation length, with more stringent request along the beam line where the design upper limit is 5%. The read-out and data acquisition system of the whole COMPASS spectrometer had been designed for high beam and trigger rate, therefore minimizing the related dead-time. Beam rates at COMPASS are as high as 10^8 Hz. The read-out rate has constantly increased up to 10^4 Hz. The read-out electronic chain of the RICH has been designed and, later, upgraded (Section 3) matching these figures.

Fig. 1 provides a scheme of principle and an artist view of the RICH. The detector [5,6] is a gaseous RICH with large transverse size to match requested specifications for the acceptance of the first stage of the COMPASS spectrometer. Hadron identification up to about 50 GeV/c is obtained with the choice of a low chromaticity gaseous radiator and with a radiation length adequate to ensure enough detected photons: particles cross 3 m of C_4F_{10} at atmospheric pressure. The choice to regulate the radiator pressure relatively to the atmospheric pressure is imposed by the two thin vessel walls in the spectrometer acceptance region, required to limit the amount of material (Section 7). The evolution of the radiator gas pressure and temperature, related to the environmental conditions, results in a corresponding evolution of the gas refractive index, taken into account in the data analysis. The control of the gas pressure and its transparency in a wide wavelength range down to the Ultra Violet (UV) domain, required by the photon detectors used (Section 6), are crucial parameters for the correct detector operation; they are ensured by the gas cleaning process and the radiator gas system (Section 4). A 21 m^2 UV mirror wall, formed by a mosaic arrangement of spherical UV mirror elements provides image focusing (Section 5). The wall consists of two (upper and lower) spherical surfaces, with the same nominal radius and different orientation (Fig. 1). This arrangement is chosen in order to focalize the Cherenkov images onto two sets of photon detectors (top and bottom detectors), with a total area of 5.3 m^2 , located outside the spectrometer acceptance, far from the beamline. This choice is imposed by the high beam rate at COMPASS. The beam rate also imposes to intercept the Cherenkov photons generated by the beam particles. A closed pipe (Section 7) with 100 mm diameter, with axis coinciding with the beam line, has been used. The large diameter is imposed by the secondary nature of the beams used at COMPASS, characterized by non-negligible phase-space size. The pipe is flushed with He to reduce the material budget along the beam direction.

Table 1

The major steps of the COMPASS RICH history. The following acronyms are used in the table: PD (Photon Detector), MWPC (MultiWire Proportional Chamber), MAPMT (MultiAnode PhotoMultiplier Tube), MPGD (MicroPattern Gaseous Detector), CLAM (Continuous Line Alignment and Monitoring method, introduced in Section 5).

| Years | Activity | Discussed in section |
|-----------|--|----------------------|
| 1994–1998 | RICH design | 2 |
| 1994–1998 | MWPC-PDs R&D | 6.1 |
| 1997–1999 | Mirror R&D | 5 |
| 1998–2000 | Radiator gas R&D | 4 |
| 1998–2000 | Constructions | |
| 2000–2001 | Commissioning | |
| 2002 | Radiator gas cleaning system in operation | 4 |
| 2002 | Fast circulation added to the radiator gas system | 4 |
| 2005–2006 | Construction and installation in the central region of PDs formed by MAPMTs coupled to lens telescopes | 6.3 |
| 2005–2006 | New electronics, APV-25 based, for the MWPC-PDs | 6.1 |
| 2004–2007 | Design, construction, installation of the CLAM system for mirror alignment monitoring | 5 |
| 2011–2012 | Construction and installation of the light beam pipe | 7 |
| 2007–2013 | R&D: novel MPGD-PDs | 6.2 |
| 2014–2016 | Construction, installation and commissioning of 4 MPGD-PDs | 6.2 |

Table 2

Perfluorobutane properties.

| Property | Value |
|---------------|--|
| Molar mass | 238.028 g × mol ⁻¹ |
| Density | 11.21 kg/m ³ (gas, 101.3 kPa at boiling point) 1594 kg/m ³ (liquid, 101.3 kPa at boiling point) |
| Melting point | −128 °C |
| Boiling point | −1.7 °C |

3. The evolution of COMPASS RICH

The RICH history is summarized in Table 1. The counter has been carefully designed and built in the last years of the 20th century and commissioned in years 2000 and 2001. The design phase has been accompanied by intense R&D activity related to the photon detectors, the radiator gas purification and the mirror system. Since then, continuous and rigorous detector maintenance has been performed.

The counter has been upgraded several times, to improve matching the demanding goals of the COMPASS physics programme and the continuously increasing trigger rate. The technological evolution in the field of photon detectors and electronics has been taken into account in these upgrade actions.

4. The radiator gas of COMPASS RICH-1 and the dedicated system

Perfluorobutane (C₄F₁₀) has been selected as radiator gas because of its high refractive index in gaseous phase at normal conditions and its low chromatic dispersion in the visible and UV domain (Fig. 2). It is in gas phase at room temperature and pressure. Other basic properties of this radiator material are given in Table 2. C₄F₁₀ has been used as radiator gas at CERN since the days of the DELPHI experiment. Therefore, a wide experience was already available at CERN and this has been largely beneficial for the use in the RICH.

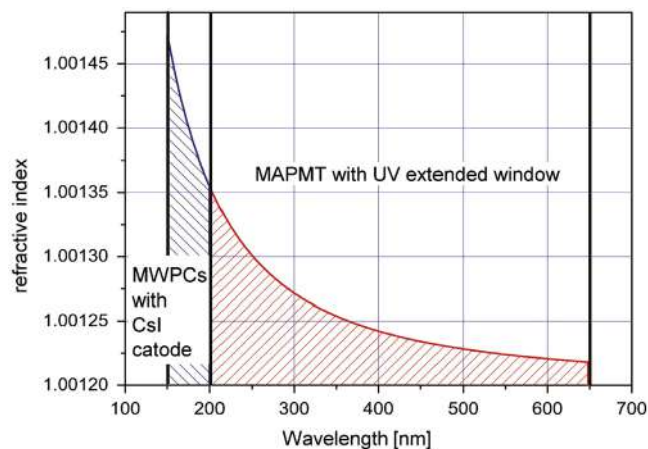


Fig. 2. Measured C₄F₁₀ refractive index versus light wavelength; data from Ref. [17]. The wavelength ranges of effective quantum efficiency for the gaseous photon detectors with CsI photo-cathodes (Sections 6.1 and 6.2) and for multianode photomultiplier tubes with extended UV glass windows (Section 6.3) are indicated.

Perfluorobutane is intrinsically transparent in the UV region. Nevertheless, the material from commercial providers can never be 100% pure and pollutants can severely affect its transparency, in particular in the UV domain. Procedures to remove the non-UV transparent contaminants have been developed [18]. The success of these approaches depends on the nature of the impurities. Among non UV transparent pollutants, oxygen, water vapour and alkenes are easier to remove, while aromatics can be removed only by lengthy procedures resulting in important material losses. The majority of the batches of 3M¹ performance fluid PF-5040, the material so far used in CERN experiments, could be made UV transparent. 3M is no longer producing the performance fluid PF-5040. For the COMPASS 2021 run, a new provider has been identified: samples of Perfluorobutane Technical-grade by F2 Chemicals² have been made fully transparent in the UV domain of interest with the procedures already used for the 3M material.

At COMPASS, a dedicated cleaning gas system, in operation since 2002, removes the pollutants of the raw material before its use as radiator gas. Perfluorobutane is circulated in closed loop in gas phase through activated carbon and 13X molecular sieve, later replaced by 5A molecular sieve. Oxygen is removed in a cool section (T: −60 °C) where C₄F₁₀ condensates and the liquid drops return to the bottle, while the gaseous component is vented out. The typical material loss is between 20% and 50% for the different batches, related to the different level of contaminants.

The radiator gas in the RICH vessel is controlled by the gas radiator system [10] (Fig. 3). The system is based on a design [19] already adopted to ensure perfluorobutane circulation in other RICH detectors, as those used in HERA-B at HERA, DESY and in the space-born experiment CAPRICE. Its main tasks are providing, during detector operation, well controlled pressure conditions in the 80 m³ RICH vessel; removing oxygen and water vapour contaminants, in order to prevent building up impurities due to leaks; performing vessel filling with perfluorobutane before a data taking period and radiator gas recovery at the end of the period. The recovery operation ensures C₄F₁₀ storage in a dedicated tank for future usage. For these purposes, the system main components are two oil-free compressors, working in parallel, which continuously extracts gas from the vessel at constant rate in order to ensure the gas circulation, a pressure sensor installed on top of the radiator vessel for

¹ Minnesota Mining and Manufacturing Company, 3M Center, St. Paul, MN, USA.

² F2 Chemicals LTD, Lea Lane, Lea Town, Preston, Lancashire, PR4 ORZ, UK.

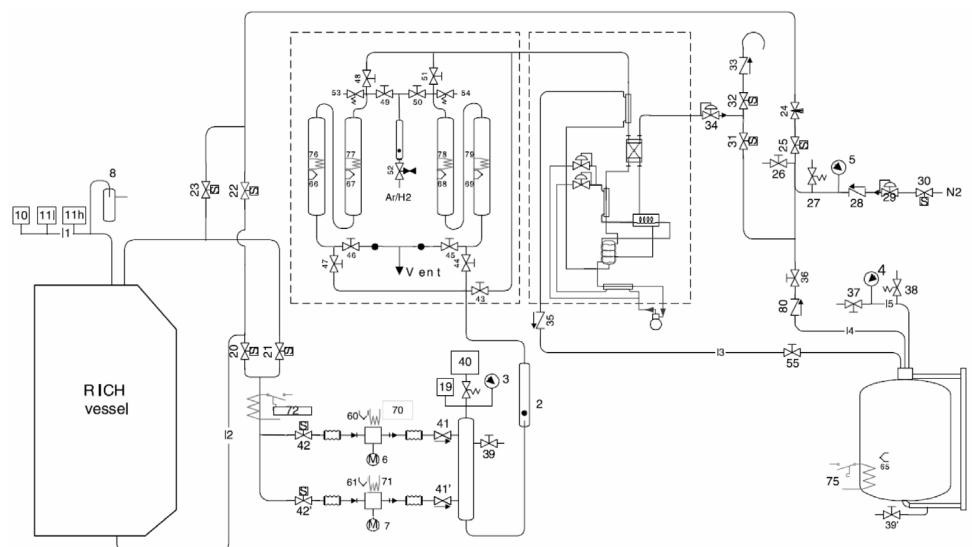


Fig. 3. Schematic diagram of the RICH gas system [10].

continuous monitoring of the internal relative pressure, a pneumatic valve on the input line, which controls the input gas flow to preserve the relative pressure inside the vessel. In fact, the pressure regulation is obtained by varying the gas flow in input to the vessel. Oxygen and water vapour traces are removed by filtering cartridges with 5A molecular sieves and Cu-catalyst, which are permanently in series in the circulation system. The vessel is flushed with nitrogen during the shutdown periods. N_2 and C_4F_{10} separation during filling and recovery is based on the different boiling points of the two gases: distillation is performed at -35°C . The pressure in the separator section is kept at 400–500 kPa: nitrogen vented out thus contains residual C_4F_{10} at the 4–5% level. The control of the whole system is performed via a Programmable Logic Control (PLC).

The gas system is complemented by monitoring instrumentation, including commercial instrumentation as a hygrometer, an oxygenmeter and a binary gas analyser and custom devices: a sonar system to determine the gas composition by measuring the speed of the sound in the gas [20] and a setup for gas transparency measurements, shortly described here. A monochromatic light beam is obtained coupling a deuterium lamp to a monochromator and detected by two Photo-Multiplier Tubes (PMT) with wavelength shifters. The monochromatic light beam enters a measuring chamber filled with the radiator gas, where the light beam is split with a beam splitter between the light detected by the reference PMT and the light detected by the measuring PMT, both read-out via picoammeters. The system can measure in the wavelength range 154–220 nm and the transmission through a path of 187 cm is measured, this being the difference in length between the paths of the light reaching the two PMTs. The estimated wavelength spread is 0.5 nm and the estimated overall absolute calibration error is ± 0.25 nm. The system is calibrated at each measurement collecting reference spectra with nitrogen. The error associated to the transmission measurements, estimated from repeated measurements, is at the 1% level.

The most relevant parameters describing the overall performance of the radiator gas system are a typical gas flow rate in the vessel of 3–5 m^3/h , a typical oxygen and water vapour contamination at a few ppm level, residual nitrogen dissolved in the perfluorobutane atmosphere in the vessel in the range 3–4%, relative pressure stable over months within 100 Pa and a typical gas transparency as shown in Fig. 4.

The relatively slow gas flow rate and the large vessel volume can result in the formation of a temperature field in the radiator volume. This effect is prevented thanks to the fast gas circulation, a parallel circulation system by a turbo-pump, in operation since 2002, that

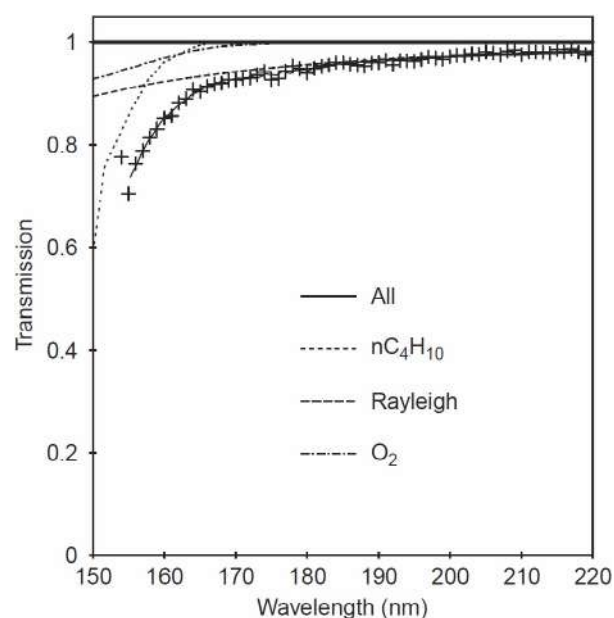


Fig. 4. Typical UV light transmission through 1.87 m of radiator gas, as measured on-line during the data taking (crosses) [6]; the fitted curve allows to disentangle the main contributions to UV light absorption, namely: Rayleigh scattering, oxygen, water vapour, hydrocarbons and alkene traces; the various relevant contributions are also plotted: they give indications on the amount of residual contaminants; in particular water vapour traces below 1 ppm and oxygen traces below 3 ppm are routinely obtained. The line at 1 is added to guide the eye.

provides gas flow at a rate of 20 m^3/h . It also contributes to reduce the overall temperature evolution of the radiator gas thanks to the use of heat exchangers.

The radiator gas system is stable, robust and easy to operate. It exhibits occasional instabilities, typically once or twice per year of operation, in case of violent thunderstorms, when atmospheric pressure increases up to 3000 Pa in less than 30 min have been observed. The circulation system is not able to provide in real time the required gas amount for compensation and an error condition is detected, causing a system halt. Recovery is by manual intervention. Regular operation is always restored in less than half an hour.



Fig. 5. The RICH mirror wall; the picture has been taken during the mirror alignment procedure [11].

5. The mirror system of COMPASS RICH

The COMPASS mirror system [11] consists of two UV reflecting spherical surfaces, with radius of 6600 mm and total area of 21 m² (Fig. 5). They are a mosaic type composition of 116 spherical mirror units: most of them are regular hexagons (side length of 281 mm) and 48 are pentagons of six different sizes, to avoid saw-teeth patterns at the central borders, between the two surfaces. The clearance between adjacent mirrors results in a 4% loss of the reflecting surface. The two spherical surfaces have centres vertically displaced, up and down, by 1600 mm with respect to the beam axis. This arrangement results in a geometrical aberration of 0.32 mrad for images produced by particles incident at small angles and larger aberration for particle incident at very large angles. The mirror substrates are borosilicate glass, 7 mm thick; their stiffness is confirmed by a Finite Element Method (FEM) calculation. The 126 substrates, including ten spare units, produced by IMMA,³ have been visually inspected and individually characterized by measuring the radius of curvature, R , and the spot diameter, D , defined as the diameter of the smallest circle containing 95% of the power associated with the image of a point-like source. The following results have been obtained: $\langle R \rangle = (6606 \pm 20)$ mm, $\langle D \rangle = (1.65 \pm 0.45)$ mm. The roughness of the polished surfaces has been checked on a sampling base: the measured roughness r.m.s. was in all cases <1.6 nm.

Good reflectance in the UV region can be obtained with a reflecting layer (Al, ~ 80 nm) and a protective layer (MgF₂, ~ 30 nm) deposited with a carefully tuned and controlled procedure, which requires very good vacuum (10^{-7} mbar), high deposition rate (2–4 nm/s) and rapid rotation of the substrate. Procedure tuning resulted from iterative

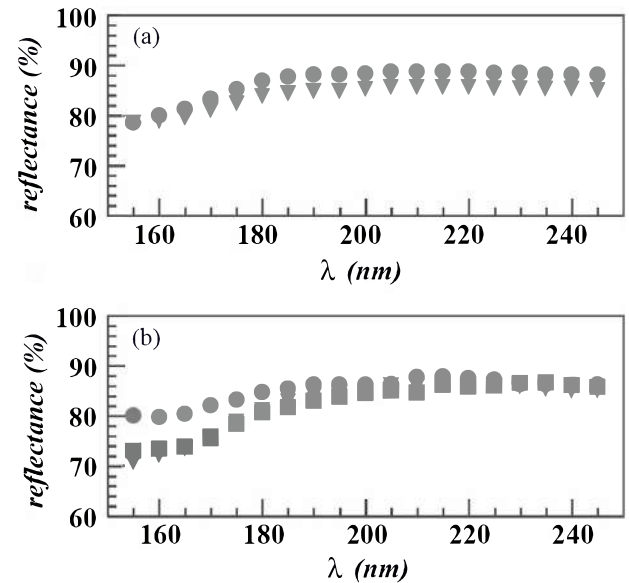


Fig. 6. (a) Mean value of the reflectance measured for the 126 mirror units at the centre (dots) and at the edge (triangles). (b) Reflectance of one mirror unit immediately after production (dots), after one year (squares) and after two years (triangles) of permanence in the RICH vessel [11].

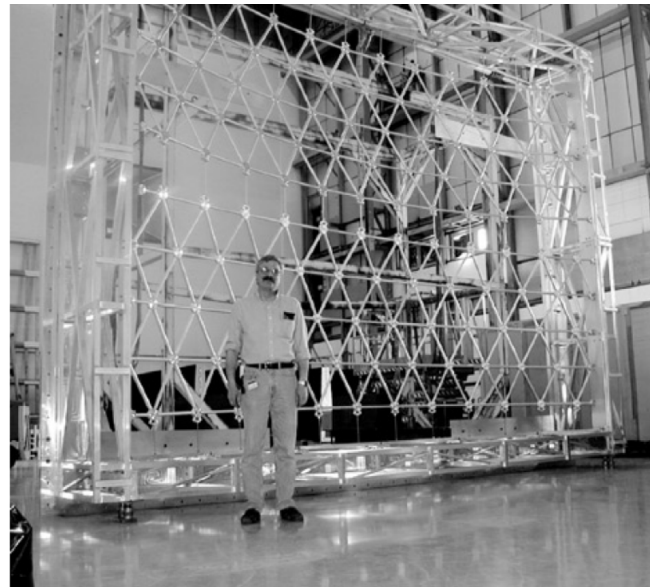


Fig. 7. The mechanical structure of the mirror wall [11].

exercises with feedback to the manufacturer⁴ from measurements at the CERN reflectometer facility [21], later also used to measure the reflectance of each mirror at the centre and at the edge. The coated mirrors must be carefully protected against humidity at all times. The measured reflectance is good (Fig. 6) with values, for wavelengths in the useful range 160–200 nm, always in the range 83–87%. Repeated measurements after 1 and 2 years of permanence in the RICH vessel indicate, after the expected short term degradation, stable reflectance.

The first element of the mechanical support of the individual mirrors, a fibreglass disc, diameter 46 mm, is glued at the centre of the mirror substrates, rear face. The substrates have a 6 mm diameter hole

³ IMMA, Ltd., Kinskeho 703, TURNOV, Czech Republic.

⁴ SESO, Pole d activites d Aix-les-milles, 305, Rue Louis Armand, 13792 Ain-en-Provence, France.

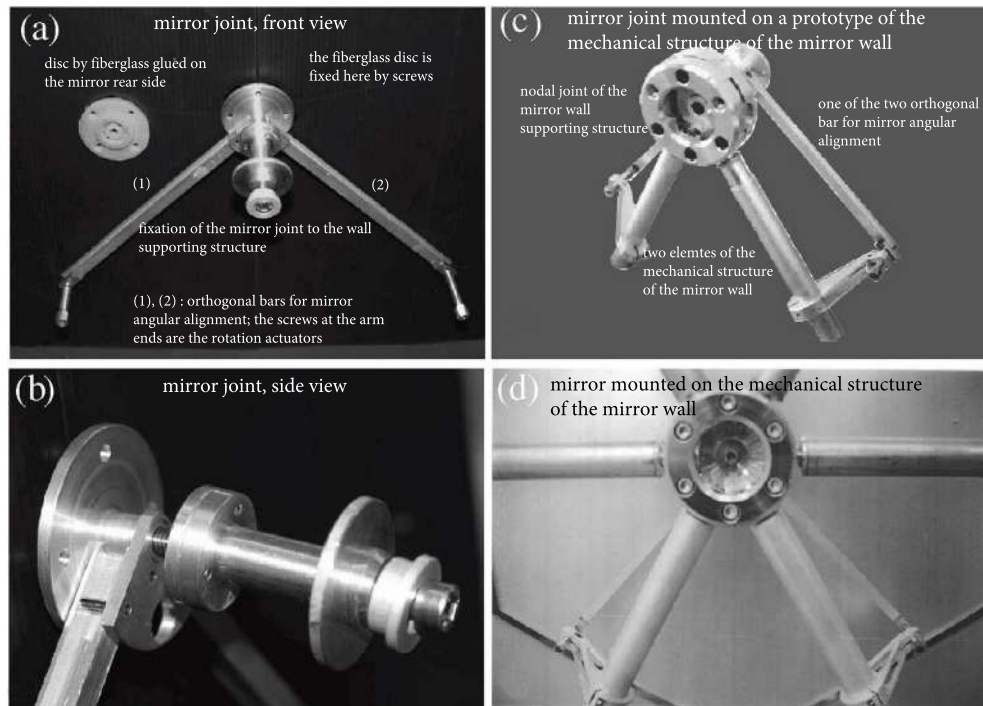


Fig. 8. (a) Mirror joint, front view; the fiberglass disc glued at the mirror rear face is also shown; (b) Mirror joint, side view; (c) the mirror joint mounted on a prototype portion of the mirror supporting structure; (d) a mirror (rear face) mounted on the supporting structure; the bars for angular regulation are visible [11].

at their centre, to allow an extra fixation, by a nylon screw, to the disc. The mechanical supporting structure of the mirror wall has a net-like configuration with nodal joints, which lay, with very accurate precision, on a sphere with the correct design radius of the mirror wall (Fig. 7). The mirrors are suspended to these nodal joints: therefore, the mirror centres are blocked on the design spherical surface. Therefore, only the angular adjustment of the mirror units is needed, ensured by the design of the joints (Fig. 8). They permit angular adjustments around two orthogonal axes by converting the translational push (or pull) of a micrometric screw; the angular resolution is 2.5 mrad/turn with very good linearity, practically no hysteresis and a negligible cross-talk of 0.01 mrad between the two rotations. Their unit weight is 112 g. Mirror angular alignment, performed after mounting the mirror units on the support structure inside the RICH vessel, is by a dedicated original procedure that makes possible to align from inside the vessel, without having visual access to the locus of the design centre of the mirror wall. The procedure makes use of a theodolite, which is positioned in front of the mirror unit under alignment. The coordinates of the sphere design centre are known in the vessel reference frame. The line joining the sphere centre and the theodolite centre, reference line, can be easily defined. The theodolite is aligned along this line. This line intercept the mirror unit in point P. The mirror unit is rotated till the normal to the mirror surface at P coincides with the reference line. When this coincidence is obtained, the normal to P points to the sphere centre, namely the centre of curvature of the spherical mirror coincides with the design centre of the mirror wall sphere. Therefore, the mirror is aligned. In practice, the alignment procedure consists in rotating the mirror till this coincidence is established. For this purpose, the theodolite optical grid is used and the mirror unit is rotated till the grid and its reflected image coincide. The upper limit of the residual misalignment angle accepted is 0.1 mrad, which is the precision achieved in defining the reference line.

5.1. Monitoring of mirror alignment

The mirror alignment cannot be verified annually with measurements inside the RICH vessel because this would imply opening the

vessel, flushing it with air to create an atmosphere adequate for the operators and mounting inside a dedicated scaffolding, so that also the most remote mirror units can be reached. This procedure causes risks of mirror degradation and other damages. Therefore, an original system for monitoring the relative mirror angular alignment without opening the vessel has been design, built and finally installed in 2007. It is based on the novel Continuous Line Alignment and Monitoring method (CLAM) [22] proposed by S. Costa and the principle is simple: the image of a reflective grid, placed inside the vessel, at the upstream face, and properly illuminated when needed, is reflected by the mirror wall. Four cameras placed at the extreme corners of the vessel upstream face collect grid images. Powerful LEDs are situated near the cameras, switched on only when CLAM images are collected. Their light, reflected by the mirror wall, illuminates the reflective grid (Fig. 9). The grid lines are expected continuous in case of perfect relative mirror alignment, while broken lines indicate misalignment and the angular deviation can be quantitatively estimated from the amount of the line discontinuity. A typical CLAM image is shown in Fig. 10. The method resolution is 0.1 mrad, also cross-checked by dedicated laboratory tests [23].

The CLAM system has monitored the stability of the mirror alignment over years, confirmed at the 0.1 mrad level. It can also answer to other relevant questions. In particular, the alignment variation before and after the vessel filling with the dense radiator gas. Disentangling between camera movements and mirror movements, it can be determined that the mirror rotation due to filling is typically 0.05 mrad in the horizontal and 0.11 mrad in the vertical direction. It could also be checked that the fast radiator gas circulation by the turbopump does not induce mirror vibrations.

Later, the potentiality of the CLAM method has been enlarged in order to perform the absolute measurement of the mirror orientation from one single CLAM picture [24,25]. For this goal, both the interior orientation of the camera, which provides the calibration, and the exterior orientation, which provides the position of the camera, are required. The interior orientation parameters and the parameters describing imaging errors are obtained by the self-calibrating bundle

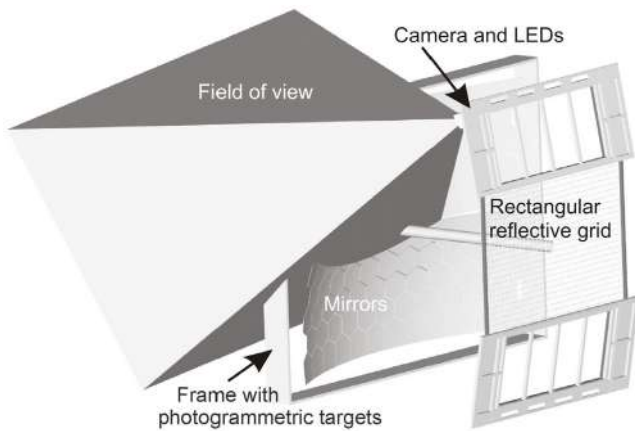


Fig. 9. The arrangement of one of the four cameras; the wall of the radiator vessel are not shown. The field of view of the camera is shown [23].

adjustment method [26]: images of a plate with circular photogrammetry targets placed in well defined positions are collected and analysed. The position of each camera was obtained by the space resection algorithm [26] using images of photogrammetric targets mounted in the vessel. The accuracy limits of the absolute measurement of the mirror orientation were determined by laser interferometry in laboratory, where a realistic geometry was simulated: they are below 0.1 mrad.

6. The detectors with single photon detection capability of COMPASS RICH

The photon detection system of the RICH has evolved in time (Table 1) following the COMPASS requirements and taking into account the evolution of the technology. During the years 2001–2004, the Photon Detection in the RICH had been performed with multiwire proportional chambers equipped with solid state CsI photocathodes (Section 6.1). Ageing and electrical stability issues related to ion backflow and photon feedback from the multiplication region to the photocathode imposed operation constraints. Multiwire proportional chambers were read-out by low-noise electronics with long integration time resulting in a $1 \mu\text{s}$ duration of the amplified and shaped signal. Moreover, also the baseline restoration time is long, of the order of

about $3.5 \mu\text{s}$. The long signal duration causes a detector memory: when a trigger occurs, signals produced in a wide time-window are registered, even if not related to the event. The long baseline restoration time generates a corresponding acquisition dead-time. In particular, the effective memory is the source of a high background level in the central region of the photon detectors, populated with the signal produced by the detected Cherenkov photons due to the high rate and extended beam halo of the muon beam. The halo particles have trajectories with very small angles respect to the beam axis, even when they are far from this axis. Therefore, the Cherenkov photons they generate are reflected in the same central region of the photon detectors. They are the source of a physical background uncorrelated with the events of interest. To overcome these limitations, and to face the higher trigger rates foreseen for the COMPASS data taking from 2006 onwards, the photon detector system of the RICH counter has been upgraded.

The upgrade of the photon detector system implemented in 2005–2006 is two-fold. The peripheral regions (75% of the surface) are populated by the images produced by lower momentum hadrons, and experience a less severe level of the uncorrelated background. Here the photon detectors are unchanged; they are read out by a new system, based on the chip APV-25, with negligible dead-time and increased time resolution (Section 6.1). The Cherenkov images produced by the high momentum particles are detected in the central photon detection area (25% of the surface), a region highly populated by the uncorrelated background. Fine time resolution to discriminate the uncorrelated background is required: this region is instrumented with a detection system based on multianode photomultiplier tubes coupled to individual telescopes of fused silica lenses to enlarge the effective active area of the photon detectors (Section 6.3).

A second upgrade of the RICH photon detector system is in operation since the 2016 COMPASS run: novel gaseous photon detectors based on micropattern gaseous detector technology replace part of the multiwire proportional chamber photon detectors (Section 6.2), in order to overcome the performance limitations of the previous gaseous photon detectors. They cover a total active area of 1.5 m^2 and they improve the stability of the gaseous photon detectors, preserving the resolution performance.

The overall arrangement of the photon detectors after the second upgrade is schematically presented in Fig. 11.

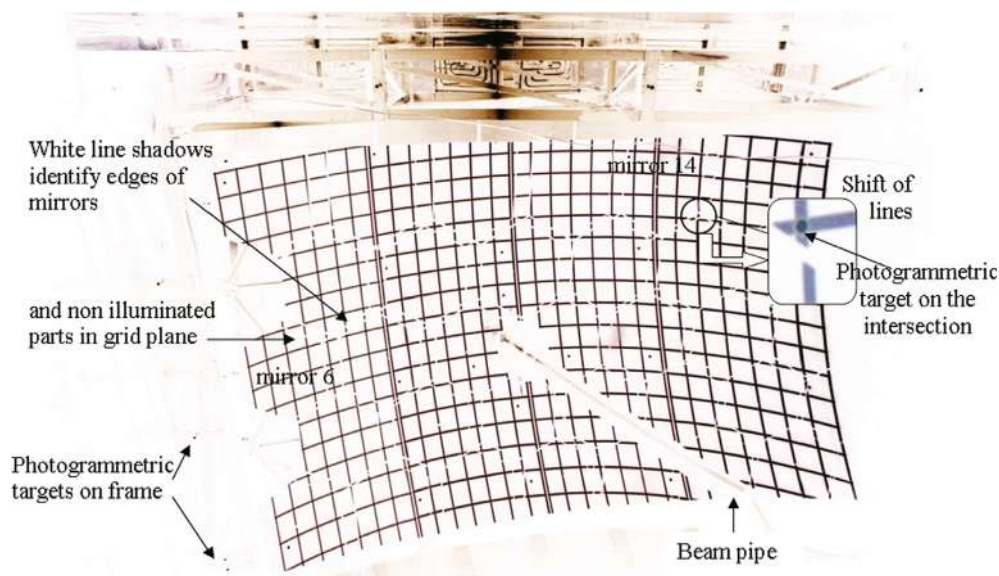


Fig. 10. A picture collected by a CLAM camera [24].

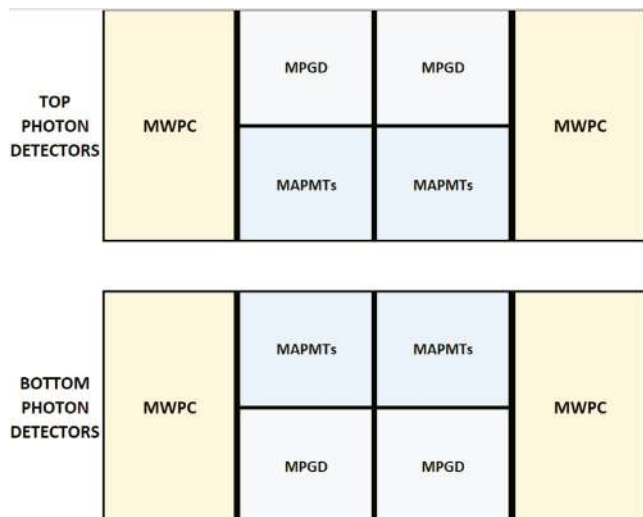


Fig. 11. Schema presenting the arrangement of the photon detectors after the second upgrade (not to scale). The following acronyms are used in the table: MWPC (MultiWire Proportional Chamber), MAPMT (MultiAnode PhotoMultiplier Tube), MPGD (MicroPattern Gaseous Detector).

6.1. The multiwire proportional chamber single photon detectors of COMPASS RICH

The surface to be instrumented with photon detectors in the RICH is as large as 5.5 m^2 , a size dictating the choice of gaseous photon detectors. In fact, the instrumentation by vacuum-based photon detectors would result too expensive. Multiwire proportional chambers, where a cathode plane is formed by a PCB segmented in pads and coated with a CsI film in order to act as reflective photocathode, represented the state-of-the-art in the field of gaseous photon detectors in the last years of the 20th century, and have been selected for the RICH. This detector architecture is the first one offering large size gaseous photon detectors with solid state photoconverter, developed within the RD26 [27] research programme.

CsI photoconverter has been selected for RD26 photon detectors because of its relatively high work function, that makes it more robust than other ones commonly used in vacuum-based detectors. When good quality fused silica windows are used, the resulting range for effective photon detection is 160–210 nm. The effective Quantum Efficiency (QE) versus the substrate and the production procedure has been optimized within the RD26 development. QE as high as typically 28% at 170 nm is routinely obtained [28] employing the facility and procedures described in detail in Ref. [29]; QE versus photon wavelength is provided in Fig. 12. The effective QE in gaseous atmosphere depends on the gas used and the electric field above the photocathode surface: photoelectron acceleration is required to limit the elastic scattering off gas molecules, which implies back scattering and reabsorption in the photoconverter. Methane and an electric field of least of 1 kV/cm provide the best performance. The choice of an architecture with reflective photocathode implies a non-critical thickness of the photoconverting film, opening the way to the production of large size photocathodes. Relative measurements of the local QE is routinely performed when large cathodes are coated with the CsI film, measuring at points forming a 5 cm-pitch grid. The QE uniformity is at the 3% level r.m.s. on cathodes as large as 0.4 m^2 .

The multiwire proportional chambers with CsI photocathode of the RICH, design according to RD26 optimization, are illustrated in the basic detector scheme presented in Fig. 13. The instrumented surface is equipped with eight identical multiwire proportional chambers, organized in two sets, the top and bottom one, each including four chambers. Each chamber (Fig. 14) has an active surface of $576 \times 1152 \text{ mm}^2$.

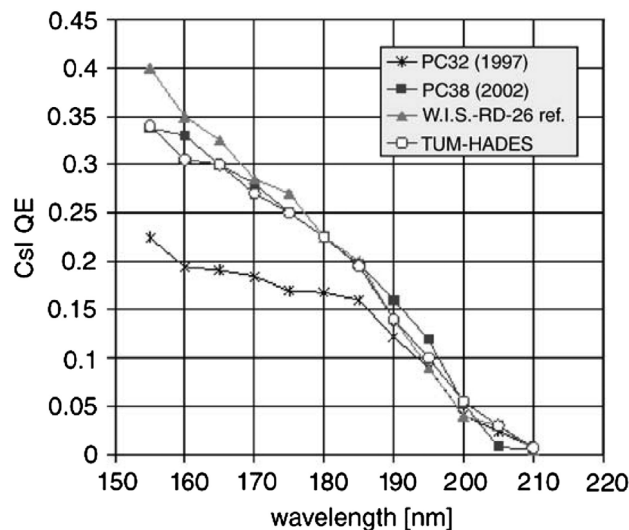


Fig. 12. The quantum efficiency of large size CsI photocathodes [28] produced at CERN for ALICE (PC32 and PC38) and at the Technical University of Munich for HADES (TUM-HADES), compared to that measured at the Weizmann Institute of Science on small samples (W.I.S.-RD26 ref.). The relevant increase of the quantum efficiency from PC32 to PC38 corresponds to the progress in optimizing the procedure to produce large size photocathode on a PCB substrate.

Two $576 \times 576 \text{ mm}^2$ double-layer PCBs, each segmented in $5184 \times 7.9 \times 7.9 \text{ mm}^2$ pads, with 8 mm pad pitch, coated with CsI, form the photocathode planes. Fused silica windows $600 \times 600 \times 5 \text{ mm}^3$ separate the radiator from the photon detectors. The anode wires, parallel to the longer detector dimension and, therefore, serving two photocathodes, have a diameter of 20 μm and a pitch of 4 mm. They are supported at mid length. The wire cathode plane is formed with 0.1 mm diameter wires, with 2 mm pitch.

The chambers, flushed with pure methane, are typically operated at 2000 V with grounded cathodes, while the collection wires are kept at 400 V, and collect the ionization electrons generated in the volume above the multiplication gap by through-going charged particles. The resulting electric field in front of the photocathodes is $\sim 7 \text{ kV/cm}$.

Till the 2004 COMPASS run, the 82944 pads of the multiwire proportional chambers have been read-out by an original read-out system with distributed intelligence [12], namely locally performing an initial data processing by FPGAs hosted in the front-end boards. Pedestal subtraction, thresholding, zero suppression and data packaging is performed at the front-end boards. The Gassiplex front-end ASIC [30] was used; it is characterized by low noise performance and long integration time (0.6 μs), resulting in a ballistic deficit of about 50%. The typical noise level measured at the RICH is 1100 electrons equivalent, resulting in an effective $4\text{-}\sigma$ threshold of 4400 electrons. Threshold value has to be compared with typical mean values of $\sim 10\text{k}$ electrons for the measured amplitude of the single photoelectron exponential spectrum, corresponding to a photoelectron detection efficiency around 60%. The long integration time also generates a detector memory, limiting the RICH performance in the COMPASS environment, where a high-rate uncorrelated background is present due to the large halo of the muon beam. The long base-line restoration time (about 3.5 μs) generates data acquisition dead-time. To overcome these limitations, since 2006 the multiwire proportional chambers have been read-out with a new system [13], based on the chip APV-25 [31], with reduced dead-time and increased time resolution, obtained by measuring three amplitude samples on the raising edge of the signal. The characteristics of APV-25 and the accurate design and implementation of the system, allow to obtain extremely good noise figures, with typical noise values of 600 electrons equivalent, exploited in $3\text{-}\sigma$ threshold values of 1800 electrons equivalent. The APV-25 chip was design for silicon trackers

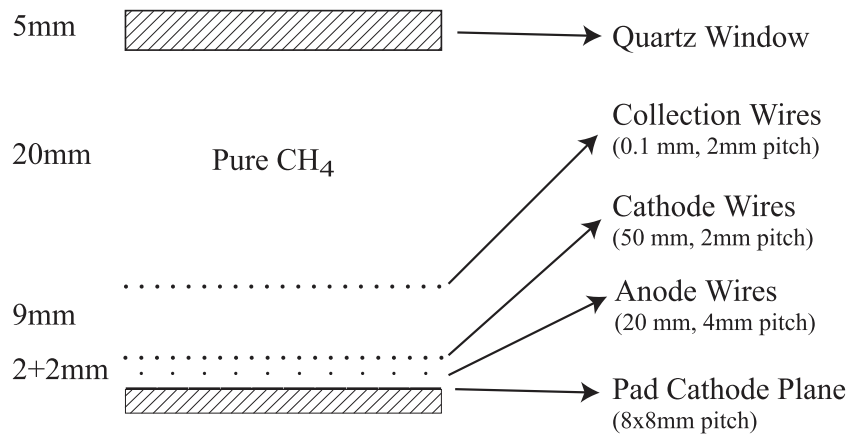


Fig. 13. Schematic cross-section of the RICH gaseous photon detectors with multiwire proportional chamber architecture (not to scale); the CsI film covering the anode pad is not shown [3].

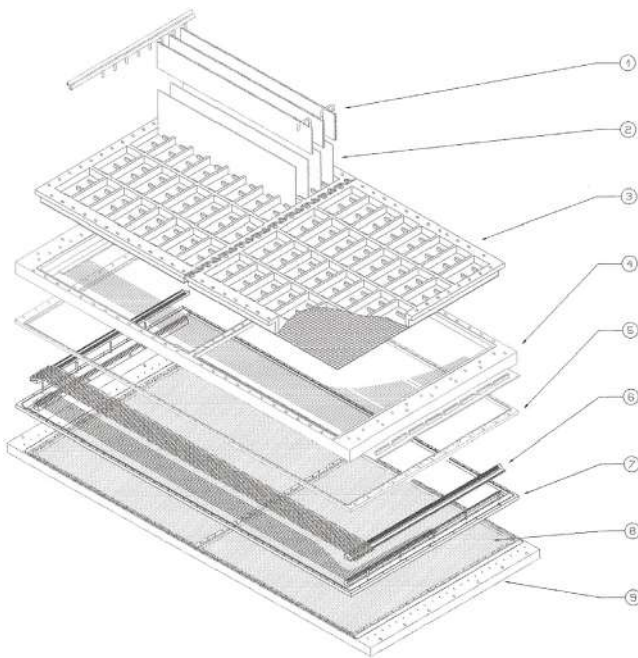


Fig. 14. One of the multiwire proportional chamber photon detectors of the RICH: (1) cooling plates, (2) readout boards, (3) CsI photocathode boards, (4) anode wires, (5) distance frame, (6) cathode wires, (7) collection wires, (8) fused silica plates, (9) fused silica frame.

and, therefore, not optimized for operation with traditional gaseous detectors. Therefore, in spite of the optimization of the configuration parameters, the ballistic deficit is large and the resulting photoelectron detection efficiency is similar to that obtained with the electronic system previously used. A typical amplitude example is provided in Fig. 15. On the contrary, there is a substantial improvement in time resolution, which is as good as 20 ns r.m.s. The APV-25 is read-out by multiplexing its 128 channels. Therefore, the effective read-out dead-time depends on both the trigger rate and the multiplexer read-out rate. A detailed study is presented in Ref. [13], from which the following numerical examples are extracted. At the multiplexed signal read-out rate of 20 MHz, used to read-out the RICH photon detectors, the percentage of lost events is 2% at a trigger rate of 20 kHz and 23% at a trigger rate of 40 kHz.

The typical number of detected photons per Cherenkov ring at saturation is 10–12, with variations among the different cathodes related to the different QE of each of them as well as to the applied voltage. In

fact, some detectors exhibit lower electrical stability, due to mechanical imperfections. The measured space resolution is dictated by the pad pitch, as the large majority of the signal clusters are formed by a single pad. The spherical aberration limits the resolution. The resulting angular resolution for single photoelectron is ~ 1.8 mrad (Section 8) and the angular resolution associated to a whole ring is 0.8 mrad.

The use over years of multiwire proportional chambers with CsI photocathodes has made possible a study of the variation of the QE versus time, over a period of six years [32]. The pollutants level in the pure methane atmosphere used in the detectors are always kept below 5 ppm of oxygen and water vapour. The absolute gain is moderate, lower than 3×10^4 and the integrated ion charge collected at the photocathode in the period under investigation is modest, less than $10 \mu\text{C}/\text{cm}^2$.

The data do not indicate any severe ageing effect: globally they are compatible with the hypothesis of no QE variation. Nevertheless, a subset of photocathodes indicate a relative QE decrease at moderate rate: 5.2% per year. The most natural hypothesis to explain a possible decrease with time of the CsI QE in gas photon detectors is a chemical or morphological evolution of the CsI film. This evolution can be related to the oxygen and water vapour contamination to which the photocathodes are exposed over years. In this hypothesis, the effect suggested by the data for a subset of cathodes can be caused by a local larger contamination level related to locally reduced tightness. No data of the contamination level in the individual detectors is available because the contamination is monitored only on a global base, measuring the oxygen and water vapour contamination of the gas on the return line, common to all the detectors.

This study indicates that CsI photocathodes used in gaseous photon detectors are robust. When they experience a low integrated ion backflow and they are exposed to atmospheres with oxygen and water vapour contamination at a few ppm level, they can preserve their QE over periods of years with at most a modest decrease.

6.2. The micropattern gaseous detector-based single photon detectors of COMPASS RICH

Four new photon detectors (unit size: $600 \times 600 \text{ mm}^2$), based on micropattern gaseous detector technology and covering a total active area of 1.5 m have replaced the previously used multiwire proportional chambers in order to improve the performance stability [14]. This is the first application of micropattern gaseous detector-based single photon detectors in a running experiment. Previously, photon detection by triple GEM detectors had been adopted for the threshold Cherenkov counter Hadron Blind Detector (HBD) [33] of the PHENIX experiment, where no single photon detection capability is needed. The micropattern gaseous detector-based photon detectors overcome

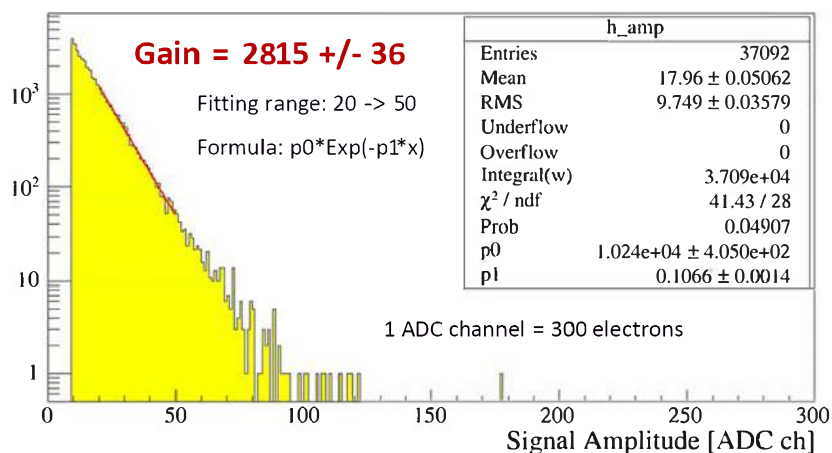


Fig. 15. Amplitude distribution measured with one of the multiwire proportional chamber read-out with the APV-25 front-end chip for a sample of hits contributing to ring Cherenkov images. The line is the result of a fitting procedure assuming an exponential distribution. The resulting gain-value is indicated with associated statistical error.

the limitations of the previous generation of gaseous photon detectors thanks to two essential performance characteristics: reduced ion and photon backflow to the photocathode, namely reduced ageing and increased electrical stability, and faster signal development, namely higher rate capabilities.

The detector architecture adopted for the RICH, is the result of a seven-year R&D activity [34]. It is based on a hybrid micropattern gaseous detector combination (Fig. 16), consisting of two layers of THick GEMs (THGEM) [35] followed by a resistive MICROMEAS [36] on a pad segmented anode. The first THGEM also acts as a reflective photocathode: its top face is coated with a CsI film. The feedback of photons generated in the multiplication process is suppressed by the presence of two THGEM layers, while the large majority of the ions from multiplication are trapped in the MICROMEAS stage. The resulting measured rate of ion backflow to the photocathode is at the 3% level. MICROMEAS properties ensure signal development in about 100 ns. Each of the four single photon detectors is formed by two identical modules 600 × 300 mm, arranged side by side in the same frame. The THGEM geometrical parameters are: thickness 0.8 mm, hole diameter 0.4 mm and pitch 0.8 mm. Holes are rimless, namely there is no uncoated area around the hole edge. They are arranged in a regular pattern with equilateral triangles as elementary cell. In order to mitigate the effect of occasional discharges, the top and bottom electrodes of each THGEM are segmented in 12 parallel areas separated by 0.7 mm clearance, each biased via an individual protection 500 MΩ resistor. Therefore, discharges only affect a single sector and the operating conditions are restored in about 10 s. The two layers are staggered, namely there is complete misalignment between the two set of holes: it is so possible to enlarge the electron cloud reaching the MICROMEAS stage, therefore favouring stable operation at larger gain in the last amplification stage.

The MICROMEAS amplifiers have a gap of 128 μm; they are built by the MICROMEAS bulk technology [37] using 0.4 mm diameter pillars with 2 mm pitch. The MICROMEAS anode is segmented in 7.5 × 7.5 mm pads with 8 mm pitch. The MICROMEAS resistivity is realized through an original implementation, where no resistive layer is applied to the pads: the resistivity is obtained by 470 MΩ resistors in series with each individual pad (Fig. 17). The 0.5 mm clearance between pads prevents the occasional discharges propagation towards the surrounding pads: the voltage drop of the anode pads surrounding a tripping one is about 2 V over the typical 600 V operation voltage, causing a local gain drop lower than 4%. The nominal voltage condition of the pad where the discharge occurred is restored in about 1 s. The detector is operated with Ar:CH₄ = 50:50 gas mixture, which ensures effective extraction of photoelectrons from the photocathode. The typical voltage applied are 1270 V across THGEM1, 1250 V across

THGEM2, and 620 V to bias the MICROMEAS. The drift field above the first THGEM is 500 V/cm, the transfer field between the two THGEMs is 1000 V/cm and the field between the second THGEM and the MICROMEAS micromesh is 1000 V/cm. The effective gain-values for the three multiplication layers are around 12, 10 and 120; these values include the electron transfer efficiency.

The novel detectors are read out by the read-out system already used for the multiwire proportional chambers with CsI photocathode.

Important effort has been dedicated to careful construction and quality control of the detector components.

The electrical stability of large-size THGEMs is a critical issue. The raw material is preselected in order to use only foils with homogeneous thickness to guarantee the homogeneity of the gain. The industrially produced THGEMs are controlled by optical inspection, by collecting and analysing microscope images, scanning by samples the large multiplier surface. A dedicated protocol has been elaborated for refining the industrially produced THGEMs, described in detail in Ref. [38]. The procedure moves THGEM breakdown voltage to at least 90% of the phenomenological Paschen limit [39]. Then, the THGEM are validated by gain maps using the multipliers in single layer detectors; gain uniformity 7% r.m.s. is obtained.

Similarly, the MICROMEAS are quality checked by collecting gain maps using an X-ray tube station; gain uniformity at 5% r.m.s. is obtained.

The quantum efficiency of the CsI photocathodes is measured obtaining maps of relative values: the uniformity within a photocathode is at the 3% level r.m.s. and among the whole production at the 10% level r.m.s. The same care and protocols already used for the photocathodes of the multiwire proportional chamber photon detectors are applied.

An essential tool for the detector commissioning and operation is the High Voltage (HV) control system [40], which also allows for voltage and current monitoring and data logging. Commercial power supplies by CAEN⁵ are used. The four detectors are organized, from the HV supply point of view, in four independent sectors each; nine different electrode types, each one with its specific role, are present in the multilayer detectors. The total number of HV channels is 136. Manual setting and control of all these HV channels would be both unpractical and unsafe. The voltages and currents of all the channels are read-out and recorded at 1 Hz frequency. During the commissioning phase, if current sparks are observed and their rate is above a given value, the voltage is automatically readjusted. During operation, the system provides automatic voltage adjustment to compensate for the variation of the environmental parameters, namely pressure and temperature,

⁵ CAEN – Costruzioni Apparecchiature Elettroniche Nucleari S.p.A., Via della Vetreria, 11, 55049 Viareggio (Lucca), Italy.

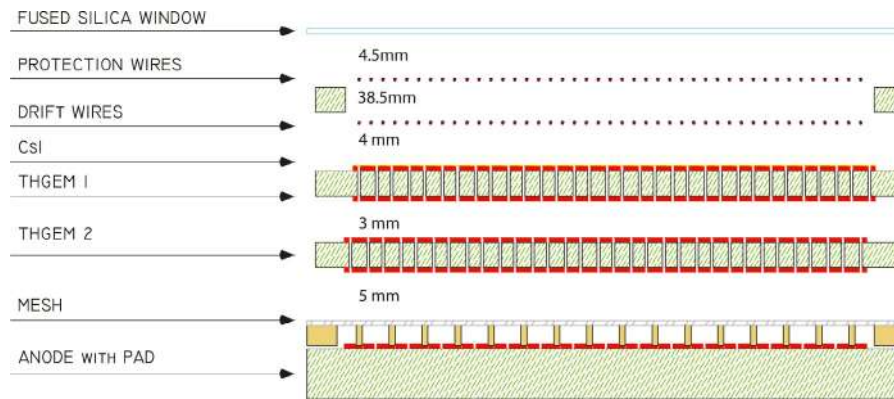


Fig. 16. Schematic cross-section of the hybrid single photon detector: two staggered THGEM layers are coupled to a resistive bulk MICROMEAS (image not to scale) [14].

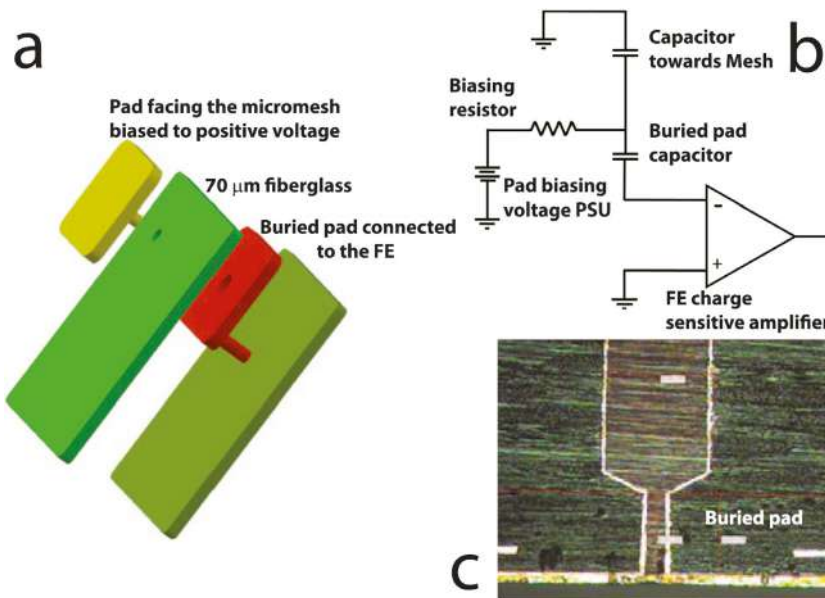


Fig. 17. (a) Scheme of the capacitive coupled readout pad. The biasing voltage is distributed via individual 470 MΩ resistors to the pad facing the micromesh structure. The buried pad is isolated thanks to a fiberglass layer and connected to the front end chip. (b) Schematic of the capacitive coupled pad principle illustrated via discrete element blocks. (c) Metallography section of the PCB: detail of the through-via connecting the external pad through the hole of the buried pad. The reduced diameter of the through-via reaching the external pad contributes preserving the pad planarity [14].

that can affect the detector gain. Gain stability at the 5% level over months of operation has been obtained.

The detectors have been used during COMPASS runs in year 2016 and 2017, for a total running period of about 12 months at COMPASS nominal beam rates. No HV trip is observed during detector operation: thanks to the resistors protecting the THGEM segments and the MICROMEAS pads, in case of occasional discharges, only current sparks, namely short-time increase of the current from the power supply, are observed, highly correlated among the three multiplication layers, which temporarily affect the local performance. The restoration after a current spark is completed within 10 s and the current spark rate is typically 1/h/detector ($600 \times 600 \text{ mm}^2$). These figures result in totally negligible dead-time related to sparks. The electronics noise, substantially uniform over the detector surface, is at the 900 electrons equivalent level (r.m.s). The images generated in the photon detectors are clean and affected by very limited background (Fig. 18). The detector resolution in the measurement of the Cherenkov angle from single photoelectrons is $\sim 1.8 \text{ mrad}$ r.m.s. (Section 8), fully matching the expectation. The angular resolution from the complete ring information is 0.8 mrad. The amplitude spectrum of the photoelectron signals is expected to be exponential. This is verified for photoelectron samples, obtained selecting hits contributing to ring images: the exponential behaviour is observed over more than two orders of magnitude (Fig. 19).

The average detector gain is extracted from a fit of the spectrum and it ranges between 13k and 14k. An electronic threshold of 3 times the noise level as measured pad by pad is applied to each read-out channel. The efficiency for single photoelectron detection is obtained from the gain and the threshold and it results higher than 80%. The noise contributing to the ring images can be estimated from the spectrum deviation from a pure exponential function at small amplitude and it is at the 10% level. A preliminary estimate of the number of detected photoelectrons per particle extrapolated to the saturation angle indicates 10–12 photoelectrons.

The high effective gain, the gain stability and the number of detected photoelectrons per ring satisfy all the requirements to ensure effective hadron identification and stable performance with the novel RICH photon detectors.

6.3. The single photon detection with multianode photomultiplier tubes in COMPASS RICH

The project, based on the use of multianode photomultiplier tubes coupled to individual lens telescopes, is extensively detailed in two dedicated articles [7,8]. The main design, construction and performance aspects are recalled in this section.

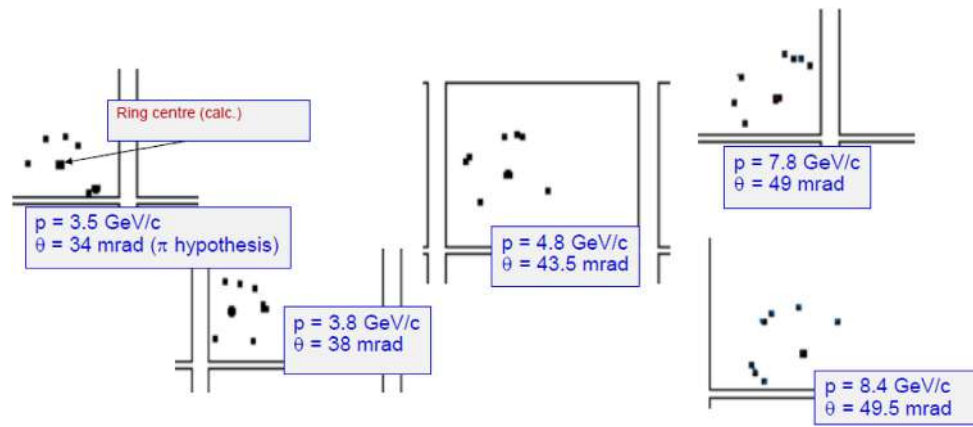


Fig. 18. Images of hit pattern in the micropattern gaseous detector-based photon detectors. No background subtraction is applied. No other filtering algorithm is applied to the images. The vertical and horizontal lines indicate the edges of the active surface of the individual detectors with size $576 \times 576 \text{ mm}^2$. The centre of the expected ring patterns is obtained from the reconstructed particle trajectories; the particle momentum and the expected Cherenkov angle of the pion hypothesis are also reported [14].

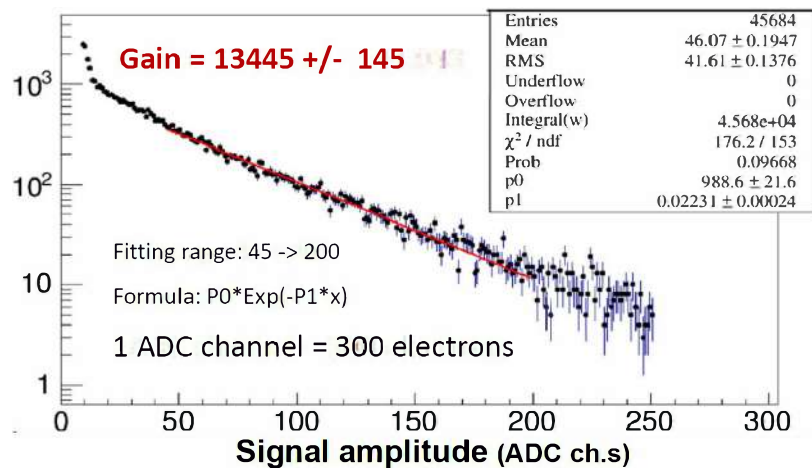


Fig. 19. Amplitude distribution measured with one of the micropattern gaseous detector-based photon detectors for a sample of hits contributing to ring Cherenkov images. The line is the result of a fitting procedure assuming an exponential distribution. The resulting gain-value is indicated with associated statistical error [14].

RICH photon detection by multianode photomultiplier tubes equipped with lens telescopes has been pioneered by HERA-B [41], where detectors by Hamamatsu⁶ had already been used. The lenses are by perspex and the two-lens telescope demagnification is 2 : 1. COMPASS design is similar, the main differences being the use of photomultiplier tubes with ultraviolet extended windows, quartz lenses and an increased demagnification.

The central portion of the RICH photon detection system, namely four panels of $600 \times 600 \text{ mm}^2$, two of them in the top detector set and two of them in the bottom set, are equipped with 576 multianode photomultiplier tubes coupled to individual fused silica telescopes (Fig. 20). The selected multianode photomultiplier tubes are Hamamatsu R7600-03-M16, 16 channels, UV extended glass window. The 16 pixels are arranged in a 4×4 matrix, the pixel size is $4.2 \times 4.2 \text{ mm}^2$ with 4.5 mm pitch. No multianode photomultiplier tube gain reduction is observed up to single photoelectron rate of at least 5 MHz per channel powering the multianode photomultiplier tubes with the standard voltage divider scheme proposed by the producer [42]. The voltage dividers implementation, where the producer parameters are preserved, is a custom realization in order to obtain a more compact setup and to save on costs. Six hundred and twelve multianode photomultiplier tubes have been submitted to a complete quality control protocol: a 2 h procedure including visual inspection, measurements of dark current

and measurements of gain at five different applied voltages. The most critical parameter is the dark current, causing a rejection rate of 1–2%.

The multianode photomultiplier tubes are mounted on the RICH in a region where the fringing field, up to 17 mT, from the first of the two COMPASS spectrometer magnets, is present. A magnetic shielding is required in order to preserve the multianode photomultiplier tube efficiency. The shielding has to reduce the magnetic field experienced by the multianode photomultiplier tubes to a value below 2 mT, a safe field level, as resulted from dedicated laboratory studies. The efficiency of each individual pixel in a multianode photomultiplier tube has been measured versus the external magnetic field. Severe efficiency reduction is observed for magnetic field exceeding 5 mT [7]. Individual soft iron boxes have been designed and built to surround the multianode photomultiplier tubes. The field inside the box has been measured for different values of the external field. For an external field of 22 mT, the internal field in the region where the multianode photomultiplier tube sits does not exceed 1 mT. The photon wavelength domain includes the visible region and the UV range down to 200 nm thanks to the use of multianode photomultiplier tubes with UV extended window and to the choice of telescopes formed by fused silica lenses. A typical example of the effective QE of the photocathodes of the multianode photomultiplier tubes, resulting from the convolution of the intrinsic QE and the window transparency, is provided in Fig. 21.

The read-out is performed by a system providing a high sensitive front-end stage, resulting in a high detection efficiency for the single photoelectron, sub-ns time resolution to minimize the background due

⁶ Hamamatsu Photonics K.K., <http://www.hamamatsu.com>.

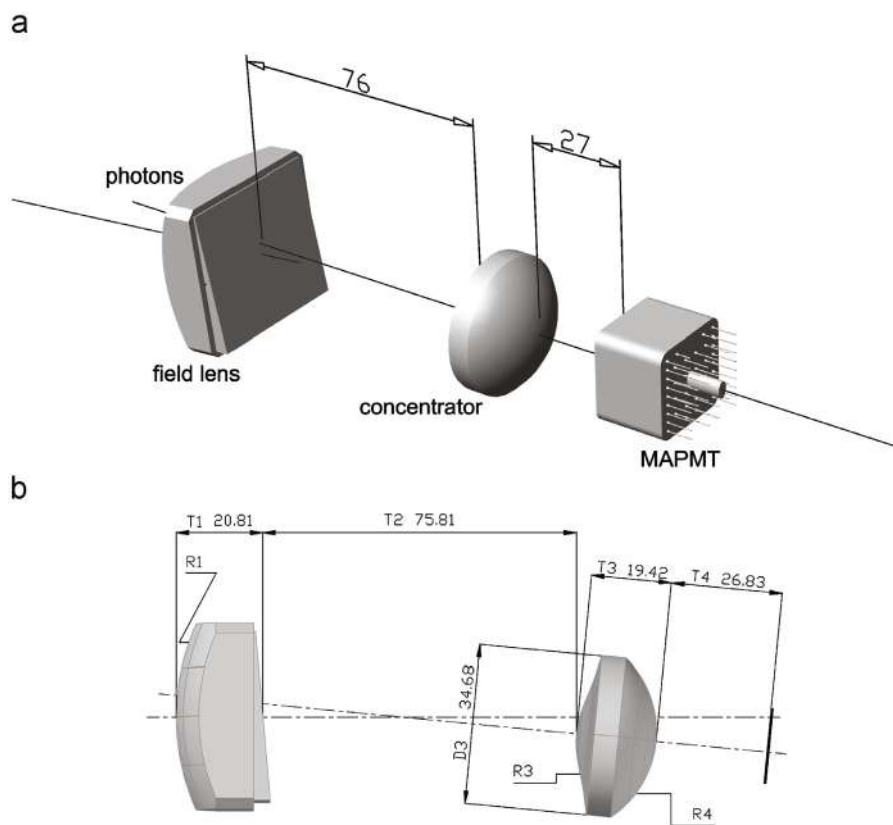


Fig. 20. The design of the telescope; (a) artistic view; (b) side view (parameters are given in mm) [7].

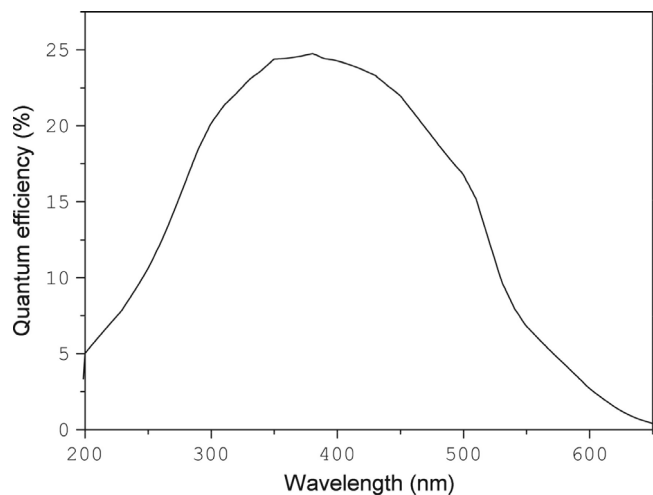


Fig. 21. Effective quantum efficiency determined by measuring the cathode photocurrent for one of the multianode photomultiplier tubes used in the RICH [7].

to uncorrelated events and to fully exploit the multianode photomultiplier tube time resolution, and high rate capabilities, as required by the high luminosity of the COMPASS experiment. It is based on the CMAD4 [43] Front-End (FE) ASIC, originally designed for gaseous detectors, and the high resolution F1 TDC [44]. CMAD4 is essential for good efficiency: it is characterized by a noise level of 5–7 fC (30–40k electrons), to be compared with a typical mean signal at FE input larger than 500 fC (3.1 M electrons), and can operate up to 5 MHz per channel. A typical amplitude spectrum obtained with a MAPMT R7600-03-M16 operated at 900 V collected illuminating the photo-cathode in single photo-electron mode is shown in Fig. 22. Various spectrum

components are clearly distinguishable: at very small amplitudes, the tail of the pedestal signal distribution is visible, followed by two signal peaks. The signal peak at larger amplitudes corresponds to the single photoelectrons that have been multiplied by the whole dynode chain of the multianode photomultiplier tube; the peak at smaller amplitude is due to photoelectrons that have escaped the first multiplication stage. The population of the lower amplitude peak is always an important fraction of the total population. For our application, the detection of the photo-electron signal of both peaks is equally important. The typical threshold setting of the CMAD4 is about 40 fC (250k electrons equivalent). This value assures the rejection of the pedestal as well as of the cross-talk signals, with minimum loss of the single photoelectrons: the single photoelectron detection efficiency of the multianode photomultiplier tube coupled to the CMAD4 chip is 95%. The digital cards housing the F1 TDCs can stably operate up to 10 MHz per channel input rate and 100 kHz trigger rate. The overall 120 ps time resolution of the read-out system guarantees negligible background level from uncorrelated physics events.

The fused silica lens telescope has been designed using ZEMAX⁷ and the following optimization figures: minimize the image distortion and maximize the angular acceptance. Another requirement taken into account is a design with at most one single aspherical lens surface in the telescope, in order to limit the cost and the production complexity. The resulting telescopes, formed by two lenses, are 11.5 cm long and have an angular acceptance of $\pm 9.5^\circ$. They are compatible with the available space of about 15 cm. The field lens has to include a wedge element to get a non-axial telescope architecture, needed because of mechanical constraints. As a consequence, we have chosen to have one of the two faces of the field lens planar, while the other surface is spherical.

⁷ ZEMAX is a commercial software package for optical system design and ray tracing by ZEMAX Development Corporation, 3001 112th Avenue NE, Suite 202 Bellevue, WA 98004-8017, USA.

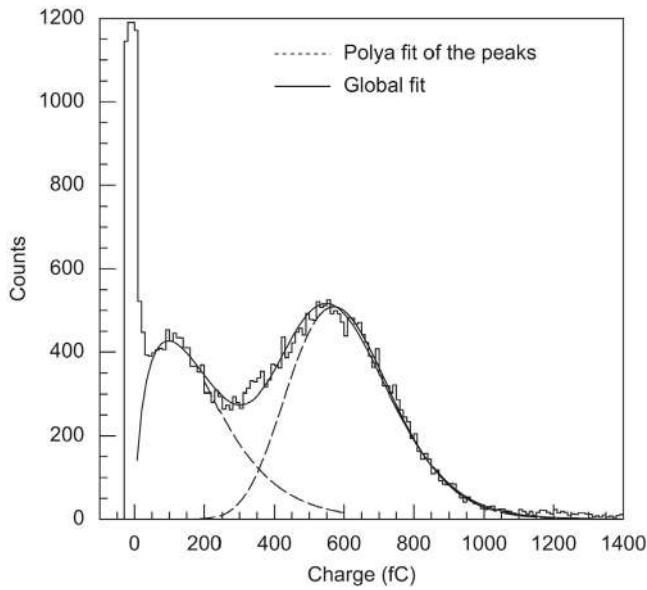


Fig. 22. Typical amplitude spectrum obtained with a MAPMT R7600-03- M16 by Hamamatsu at 900 V illuminating the photo-cathode in single photo-electron mode. The noise pedestal is visible, as well as two signal peaks, the lowest one corresponding to photo-electrons skipping a multiplication stage. The dashed curves are individual fits of the two peaks with Polyfit functions; the solid curve is a global fit with a sum of two Polyfit functions [8].

The concentrator lens has a spherical and an aspherical surface, which guarantees a minimum image distortion, even if it imposes production issues. The image demagnification is large and the ratio between the telescope entrance window and the active multianode photomultiplier tube surface is larger than 7. The resulting effective pixel size is $10.7 \times 10.7 \text{ mm}^2$ with 12 mm pitch. Two achievements are obtained thanks to the large demagnification and the accurate arrangement of the multianode photomultiplier tube and the lens mechanical supports: it is possible to save on the number of multianode photomultiplier tubes required, and to cover $\sim 98\%$ of the surface with the field lenses, thus limiting the dead area between the individual telescopes. The spot size

is $\sim 1 \text{ mm}$ r.m.s., taking into account the chromatic effects and the angular acceptance.

Each individual lens and each assembled telescope have been controlled employing the Hartmann method [45]. This method is based on the use of a mask with a regular array of holes, placed at the pupil of the optical system to be tested (Fig. 23). A parallel beam illuminates the optical system through the mask. The image of the spots corresponding to the holes is collected at a defocusing position. The shape of the wavefront can be deduced from the spot image: the aberrations of the optical system can be determined, comparing the reconstructed wavefront with the ideal one. To measure accurately the position of the spots, the defocusing and the separation of the holes have to be quite large to avoid overlapping spot images. The setup (Fig. 24) and the code for the Hartmann tests are custom-made. The image displacement introduced by optics imperfections is below $50 \mu\text{m}$ for 70% of the telescopes, below $100 \mu\text{m}$ for 20% and below $150 \mu\text{m}$ for the remaining 10%.

The multianode photomultiplier tubes coupled to the individual telescopes are arranged in 600×600^2 panels (Figs. 25, 26).

The multianode photomultiplier tube photon detectors provide an overall measured time resolution of 1 ns r.m.s., where the major limit to the resolution figure is due to the different geometrical path length of the Cherenkov photons.

The average number of detected photons per ring is about 56 for saturated rings. The resolution on the measured Cherenkov angle using single photon information is 2 mrad r.m.s., using the whole collected information is 0.3 mrad r.m.s. The two resolutions scale reasonably well with the square root of the number of photons, confirming the negligible effect of the residual background achieved thanks to the fine time resolution. The very limited residual background is also proven by the RICH performance for particles at small scattering angles, namely with images in the region largely affected by the background due to the muon beam halo. With reference to the analysis algorithms (Section 8), no efficiency reduction is observed for particle scattered at small angles, in spite of the fact that the related Cherenkov images are formed in a photon detection area where the photon flux is extremely high: up to 1 MHz per channel. This is shown in Fig. 27, where the efficiency obtained with the upgraded counter is compared with the efficiency figures obtained before upgrading the RICH with multianode photomultiplier tube-based photon detector panels.

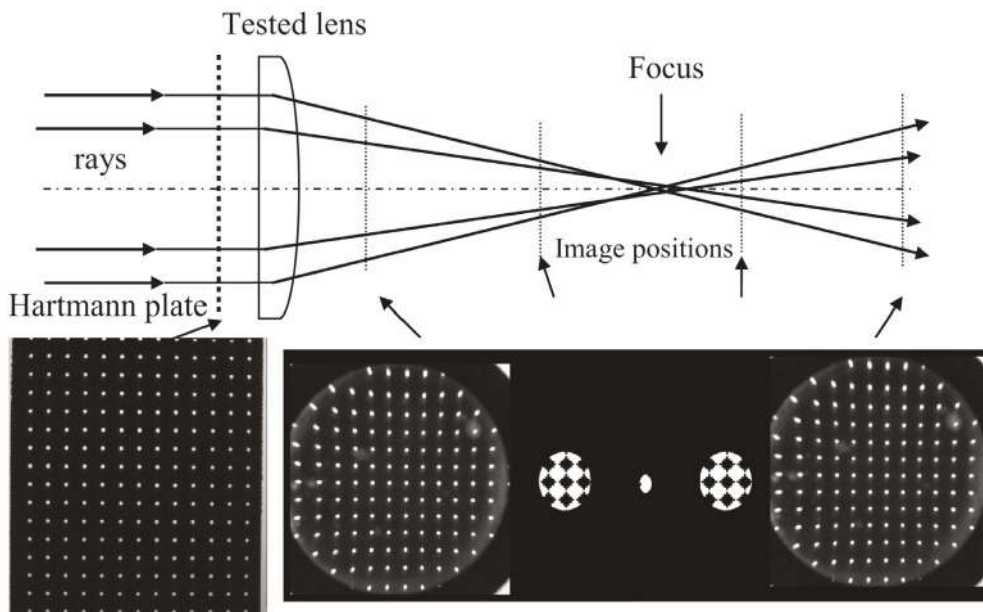


Fig. 23. Schematic illustration of the principle of the Hartmann method [7].

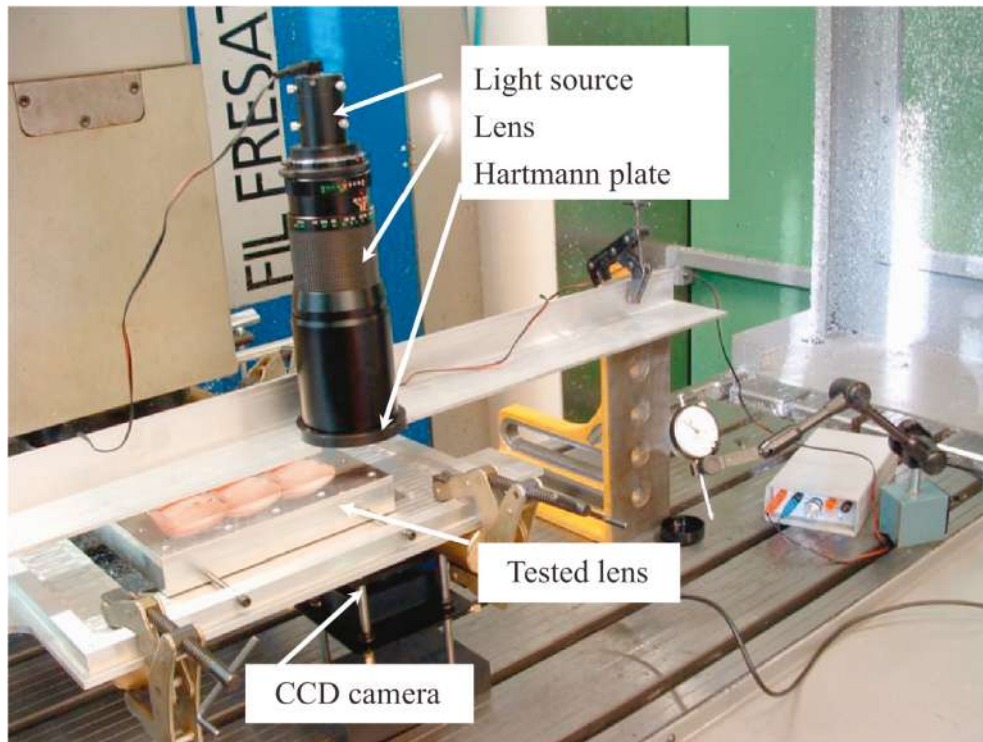


Fig. 24. The setup built for the assessment of the optical quality of the telescope elements and the correct telescope mounting [7].

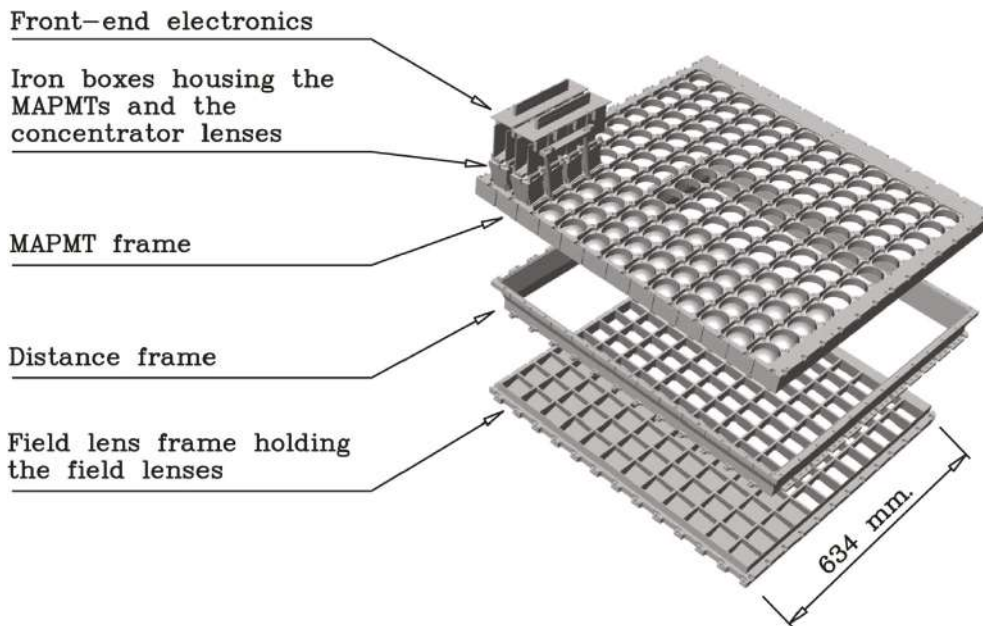


Fig. 25. The three frames that assembled together form the mechanical structures of one of the four multianode photomultiplier tube panels; from bottom to top: the field lens frame, the distance frame and the multianode photomultiplier tube frame [7].

7. Material budget

Attention has been paid to minimize the material budget, in particular in the beam region, namely at radial distance <5 cm from the beam line, where the requirements are more stringent.

Outside the beam region, the two major contributions to the material budget in the acceptance are the radiator ($10.5\% X_0$) and the mirrors ($5.5\% X_0$ for the substrates, $2.5\% X_0$ for the mechanical supports); the front and rear vessel windows are sandwiches of two thin

Al foils and a layer of rigid foam, resulting in $2\% X_0$ per window. The total material budget is $22.5\% X_0$.

In the beam region, mirrors are not present thanks to an opening in the mirror wall, the front and rear vessel windows are locally modified removing one of the Al foils and the foam, the gas radiator is present for a limited length of 24 mm, thanks to the beam pipe filled with He. The thickness of the pipe front and rear windows is, in total 0.3 mm of steel. The resulting material budget is as low as $2.4\% X_0$. The thickness of the lateral pipe wall is 0.1 mm only. Nevertheless, the reaction products emitted at very small angles, can experience a substantial path in the

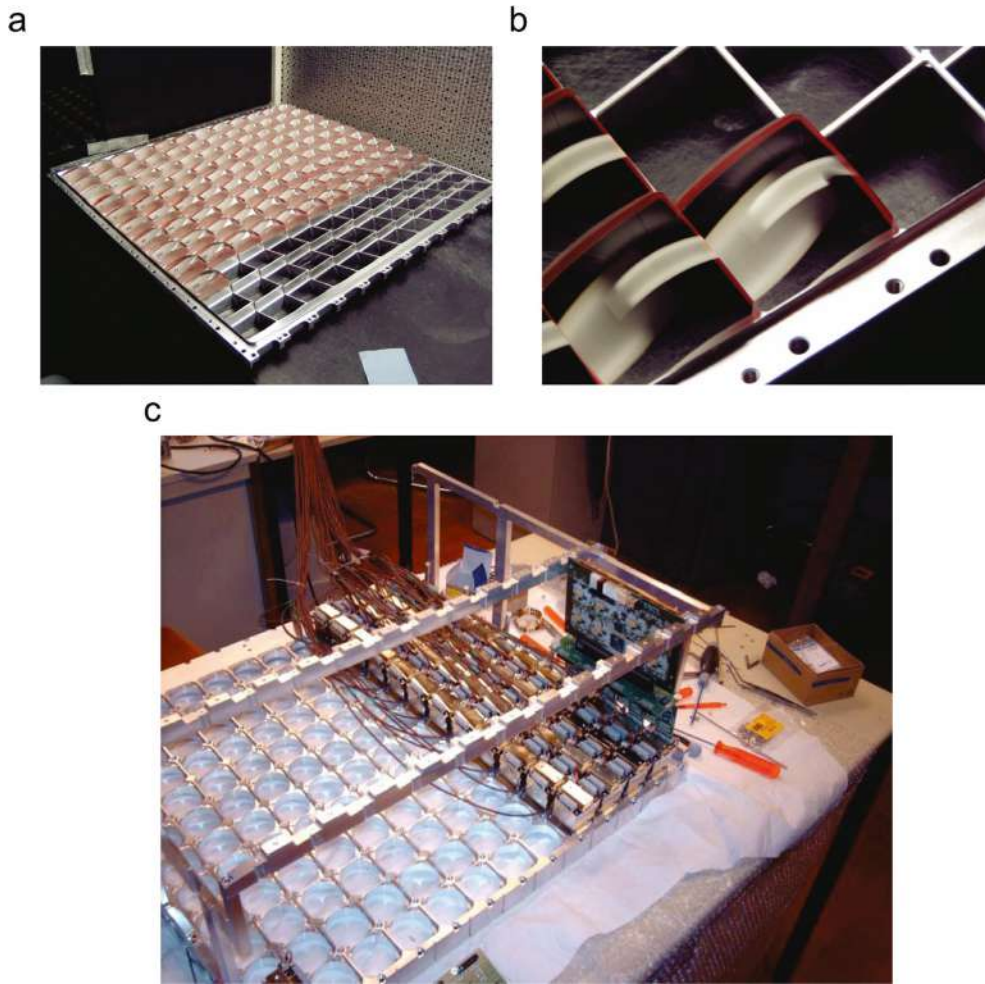


Fig. 26. Pictures of the mechanical structure components of one of the multianode photomultiplier tube panels; (a) the field lens frame partially equipped with lenses; (b) detail of the field lens frame; (c) the multianode photomultiplier tube frame partially equipped with the iron boxes housing the multianode photomultiplier tubes and the concentrator lenses [7].

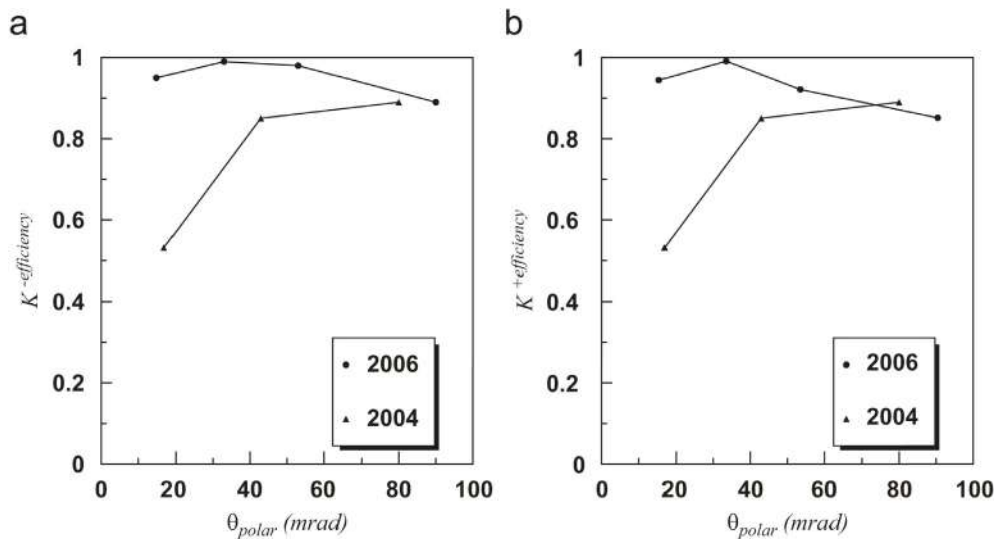


Fig. 27. PID efficiency versus polar angle for a sample of K_s from ϕ_{1020} decay; ϕ decay events are selected using the kinematic reconstruction; (a) K^- ; (b) K^+ . 2004 data have been collected before the upgrade of the RICH photon detector central region; 2006 data have been collected after implementing the upgrade [7].

pipe wall, affecting, in particular, gammas in the forward direction. The new beam pipe formed by four layers of 25 μm stretched polyester film with a 50 nm Al coating, has allowed overcoming the limitation. The

pipe front and rear windows are also by aluminized polyester. After 2012, when the new beam pipe had been installed, the material budget in the beam region decreased to about 1.4% X_0 .

8. Particle identification with COMPASS RICH

RICH data reduction [9,46] is performed using the dedicated software package RICHONE, designed, realized and constantly updated in order to follow the detector upgrade. RICHONE performs pattern recognition, Particle IDentification (PID), detector performance studies, as well as tuning and calibration tasks. RICHONE is part of CORAL, the COmpass Reconstruction and AnaLysis package [3], which is an object oriented program, written in C++, with modular architecture. The algorithms have been optimized for the reduction of COMPASS data, where the charge particle multiplicity per event is low (Section 2) and, after the 2005–2006 upgrade, the background level is low, as also tested by the occupancy levels: in the MAPMTs, the single channel occupancy is lower than 1%; in the gaseous detectors, it is lower than 0.1%.

The flow of RICHONE is based on three main steps.

The reconstructed coordinates measured by the RICH photon detectors are photon candidates. A Cherenkov angle is calculated for each photon candidate and each particle trajectory reconstructed by CORAL. This step provides the input for the following ones.

Using the calculated values of the Cherenkov angle provided by the photon candidates and the particle momentum, the value of a likelihood function is computed for each relevant mass hypothesis and for the hypothesis of absence of signal, namely mere background. The extended likelihood method [47] is used. Its application to the RICH data reconstruction is reported in detail in [9]. For each accepted particle, the PID procedure is applied independently, disregarding the other particles of the same event. This individual particle approach is adequate at COMPASS where the charge particle multiplicity per event is low. Knowing the refractive index and the particle momentum, for each mass hypothesis, the expected Cherenkov emission angle is computed. Cherenkov photons from the other particles in the event, signals from out-of-time hits and from detector and electronics noise give origin to the background. A fiducial region is defined, keeping only photon signals with angle respect to the particle trajectory smaller than 70 mrad, to be compared with the maximum Cherenkov angle of 55 mrad. The extended likelihood function includes terms related to the angle of the photon candidates in the fiducial region, to the number of photons following the Frank–Tamm distribution previously normalized from the data, and to the background distribution in the photon detectors, previously extracted from the data themselves. The extended likelihood function is computed for five mass hypotheses (e, μ , π , K, p) and for the background hypothesis. The likelihood value is used for hypothesis testing; at the first order the maximum of the six values is assumed to correspond to the good hypothesis; more elaborate evaluations, based on the ratios of likelihood values for different hypotheses, are also used in the analysis.

The extended likelihood function is also computed as a function of the mass hypothesis, assumed as a continuous parameter; the angle computed assuming for the mass the value for which the function is maximum is taken as the estimation of the Cherenkov angle of the considered particle provided by the likelihood approach.

This algorithm is the basis of the PID used in the analysis of the experiment results.

In parallel and independently from the likelihood calculations, a pattern recognition is performed, to extract the Cherenkov photons emitted by the particle, on the basis of the expected pseudo-ring image. The recognized patterns are referred to as rings.

The algorithm aim is to select from all the reconstructed photons relative to a particle those which belong to the signal, namely the Cherenkov photons emitted by that particle. The distribution of the angle of all the photon candidates relative to a particle up to maximum value set at 70 mrad is scanned using a fixed width window, counting the number of photons inside the window and looking for the angle value for which the number of photons is maximum. Cherenkov photons are expected to have a Gaussian-like distribution around the value

of the Cherenkov emission angle. The window has typically a width of ± 2 times the r.m.s. of the gaussian distribution. We assume that most of the signal is inside the window of maximum content and we take these photons to define the ring. The ring angle is then computed as the average inside the window. A simplified PID form is obtained evaluating the ring χ^2 comparing the measured angles of the photons in the ring with the angle calculated for a given mass hypothesis and repeating the calculation for all the relevant particle masses. The sum over the photons of the ring is without distinction between signal and background.

The ring recognition algorithm has been used mainly to tune the RICH response and to cross-check on statistical basis the PID results, as well as for detector characterization.

The approach adopted for the RICH data reduction presents similarities and differences respect to other approaches, that had been developed during the same years. In particular, fruitful synergies came from developments for the LHCb RICH system. The design of this software package [48], has a structure similar to the COMPASS one, including two different and parallel steps: a local pattern recognition based on ring image reconstruction and a PID performed using a likelihood function. At variance with the likelihood function used in COMPASS, the LHCb likelihood function is a global one, which includes the information relative to all the trajectories in an event. This global approach is imposed by the high track multiplicity in LHCb events. The analysis of Cherenkov rings in HERA-B RICH [49] is also based on a maximum likelihood approach, enriched with an iterative procedure: the method, namely an iterative sorting of hits on the photon detector, is particularly useful for events where rings overlap considerably, at it is the case in the HERA-B RICH, due to the high track multiplicity of the events.

The measured Cherenkov angle associated to a particle is determined from the reconstructed photon angles, either using the likelihood-based method or the ring reconstruction method. Fig. 28 presents the measured ring Cherenkov angle as function of the particle momentum.

A key ingredient for PID is the precise knowledge of the effective refractive index n , that can only be extracted from the data collected with the RICH. It depends on many parameters, mainly on the purity of the gas, the pressure and the temperature. Thus its value is time dependent. For each photon associated to a particle of measured momentum, n is computed from the Cherenkov equation, assuming the π mass. The distribution of such values exhibits a Gaussian-like peak over a background (Fig. 29). The mean value of the Gaussian best fit of the peak is assumed as the index value. The data from multianode photomultiplier tubes and the data from the gaseous detectors provide two different values of n , because of the different wavelength range of the detected photons. n must be known with high accuracy: a Δn of 10^{-5} with respect to a reference value of $n = 1.00150$, namely a variation of the order of 1% in $(n-1)$, corresponds to a variation of the Cherenkov angle of the order of 0.2 mrad. Temperature and pressure oscillations causing $(n-1)$ variations at the 2% level or more are regularly observed, even induced by the day and night excursion of the environmental parameters. They require a continuous adjustment of the n -value for data processing. A double data reconstruction, once to extract n and a second one to process the data with the correct n -value cannot be afforded. In fact, sizeable changes of the refractive index are observed every hour. In order to follow the refractive index evolution versus time extracting it from the data, a sample of data collected every hour should be analysed. This corresponds to the need of analysing twice approximately 10% of the collected data. The load is heavy, taking into account that COMPASS typically collects a few TB of data per day. Therefore, n is measured from a limited number of data samples and the evolution of its value is calculated from the measured temperature and pressure parameters. This approach provides $(n-1)$ -values accurate at the per mil level (Fig. 30).

The detector performance is demonstrated by the excellent angular resolution and the number of detected photons.

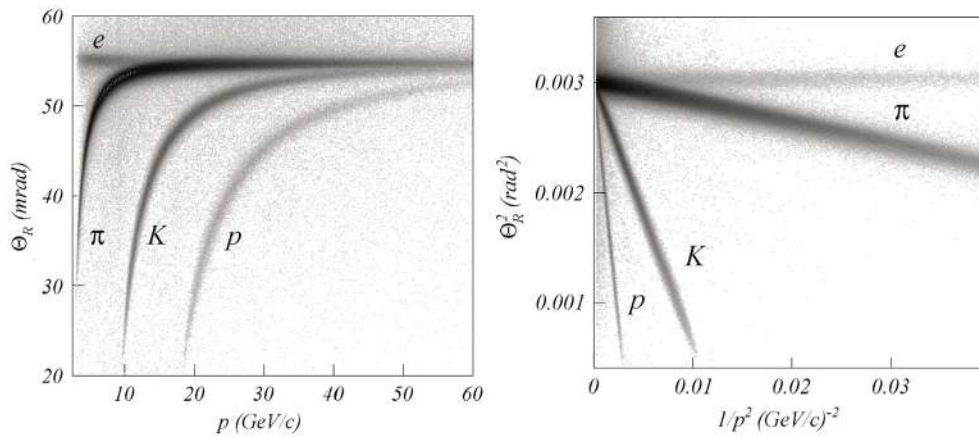


Fig. 28. The measured ring Cherenkov angle θ , as reconstructed with the pattern recognition algorithm, versus the particle momentum p (left), and θ^2 versus $1/p^2$ (right) [9].

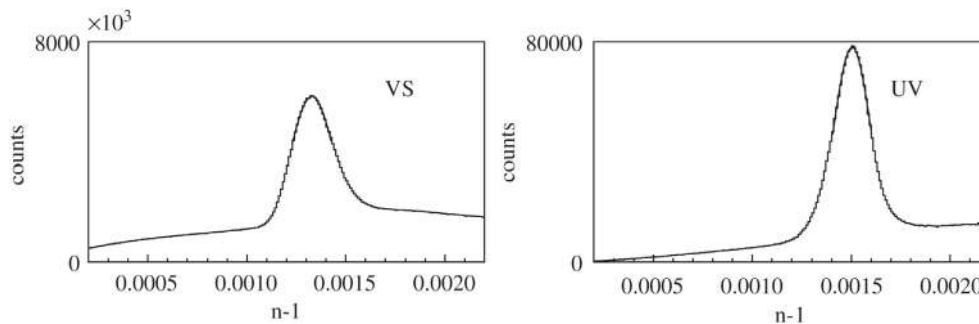


Fig. 29. Distribution of the refractive index value calculated for the detected photons assuming the π mass [9]. Left: MAPMT data, visible and near UV photons; right: gaseous detector data, far UV photons.

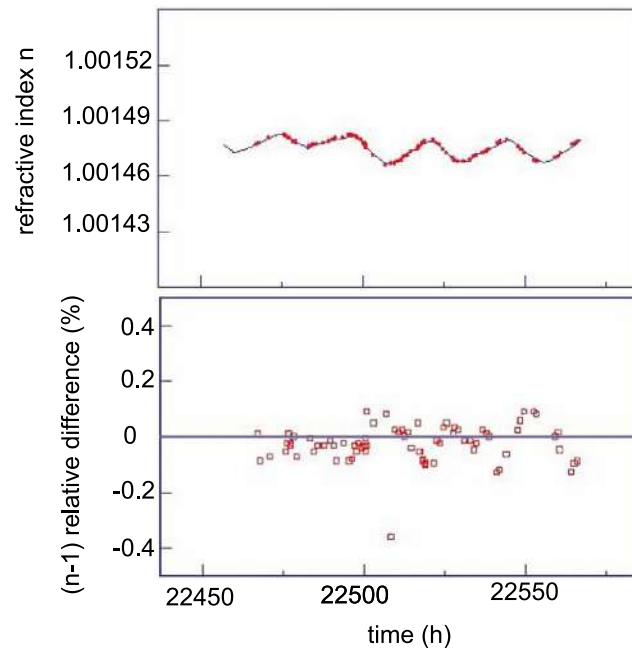


Fig. 30. Refractive index for the gaseous photon detectors. Top: The measured refractive index n versus time (open squares) and the refractive index calculated from the temperature and pressure evolution (continuous line). Bottom: the relative difference of $(n-1)$ from the measurements and from the calculation. The time scale refer to the COMPASS experiment clock including all the data taking periods collected over years.

The distribution of the difference $\theta - \theta_\pi$, where θ is the reconstructed Cherenkov angle and θ_π is the Cherenkov angle calculated from the particle momentum assuming the π mass is shown in Fig. 31. The only

selection applied is by requiring that the maximum value of the likelihood function, among those calculated for the different hypotheses, corresponds to the π mass hypothesis. All the photons in the fiducial

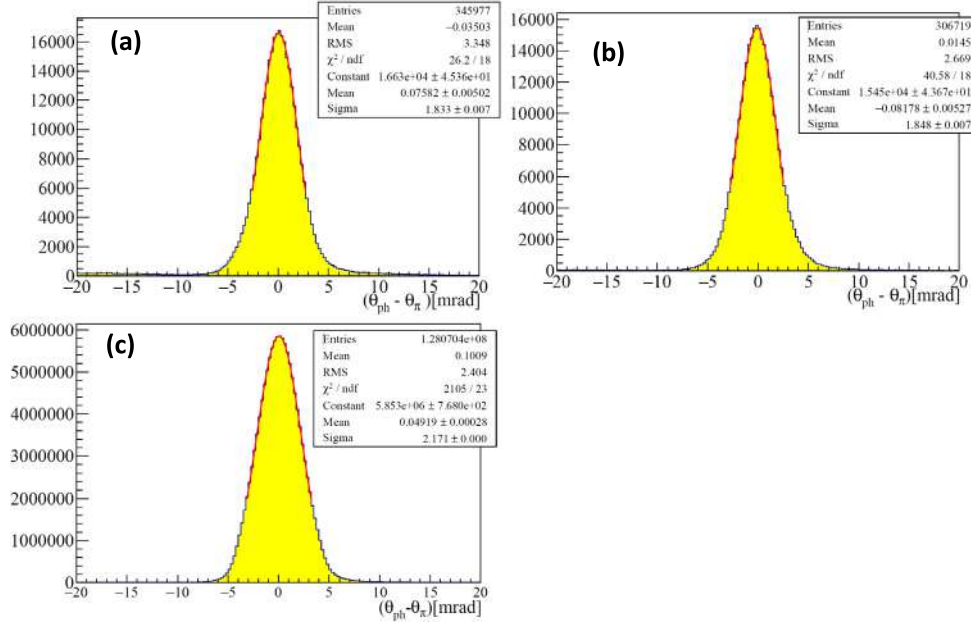


Fig. 31. $\theta - \theta_x$ distributions for all the photon detected in the fiducial area; particles are selected requiring that the maximum value of the likelihood function corresponds to the π mass hypothesis. A gaussian fit of the central peak is superimposed to the distribution; (a) multiwire proportional chambers; (b) micropattern gaseous detectors; (c) multianode photomultiplier tubes.

region, namely up to 70 mrad, are included. The distributions are separately shown for photons detected in the three different photodetector types. The distribution width is the same for the two gaseous detector types, as expected, because the pad size, the chromatic dispersion are the same and the spherical aberration is similar. The slightly larger distribution obtained with the multianode photomultiplier tubes matches the expectation, because of the larger effective pad-size and the chromatic dispersion, while the spherical aberration is negligible in the region equipped with these detectors.

Fig. 32 presents the distribution of the mean number of photons per ring from the pattern recognition algorithm as function of the Cherenkov angle for two gaseous detectors of different type. The number of emitted Cherenkov photons follows a Poissonian statistics. We assume that also the number of detected Cherenkov photons follows the same distribution. The minimum requirement to have a reconstructed ring is to have at least one associated photon. This fact implies that the Poissonian distribution of the number of photons is not complete because zero-photon rings are not taken into account: the mean value is biased towards larger values. This bias is evaluated and the average number of photons is corrected correspondingly [32]. The distributions of the average number of photons versus the Cherenkov angle are fitted with the following function:

$$N(\theta) = p_0 \cdot \sin^2(\theta) + p_1 \cdot \theta \quad (1)$$

where $N(\theta)$ is the average number of detected photons, p_0 and p_1 are the coefficient to be determined with the fitting procedure. The first term in Eq. (1) describes the number of signal photons following a Frank and Tamm shape. The second term describes the background contribution with a linear dependence on the angle as suggested by geometrical considerations: the data show that the background photons are distributed uniformly in the detectors. Similar numbers of photons for the two gaseous detectors, namely 10–12 per ring at saturation, result from the fitting procedure: the smaller active area of the photocathodes of the micropattern gaseous detectors due to the THGEM holes is compensated by the larger gain of the micropattern gaseous detectors which ensures larger efficiency of photoelectron detection. The estimated background level is in the range 20–30% of the signal. Many more photons per ring are detected with MAPMTs; this is related to their much wider quantum efficiency wavelength range. A

similar approach to estimate the number of photons at saturation when multianode photomultiplier tubes are used is not possible, because the probability to detect more than a single photon in a pad is non negligible, in particular near saturation. This effect reduces the number of resulting photon signals respect to the number of detected photons. Nevertheless, the detector performance is related to the photons signals. At saturated Cherenkov angles, the measured number of signal photons is 56 and the background level is around 30% of the signal. The probability that more than one photoelectron produces a signal over threshold in the same pad is non negligible. In this case, a single photon is counted. This reduction is included in the expected number of detected photons.

PID is based on the values of the likelihood function evaluated for different mass hypotheses and for the background hypothesis. The mere use of the highest value of the likelihood function L is, in general, a too crude approach and compromises the identification purity, that can be improved by requiring the ratio of the likelihood with respect to the background hypothesis L_{back} , or to the second highest likelihood L_{2nd} to be above a given threshold. A cut in the ratio L/L_{back} helps when a small number of detected photon is expected, namely near the threshold of the Cherenkov effect or in regions where part of the photons cannot reach the photon detectors, as it is the case for particles emitted in the very forward direction, where part of the Cherenkov photons are screened by the beam pipe. A cut in the ratio L/L_{2nd} is adopted in order to have cleaner samples at high momenta, where the Cherenkov angles for different mass hypotheses, and consequently the likelihood values, are very close. In general, efficiency and purity depend strongly on the chosen cuts. The threshold for these cuts are usually tuned for the specific analysis to find a good compromise between the efficiency and the purity of the sample according to the needs. This concept is demonstrated in Fig. 33 using samples of pions and kaons from K_S and Φ_{1020} decay.

Hadron identification is central for COMPASS physics programme [1], where RICH contribution is mandatory for the nucleon spin physics (gluon polarization from open charm muoproduction, flavour separated helicity Parton Distribution Functions (PDF), Collins and Sivers asymmetries for pions and kaons, dihadron asymmetries with hadron identification, Λ polarization transfer), in hadron production studies (D^* and D meson production, multiplicity ratio, multiplicities of

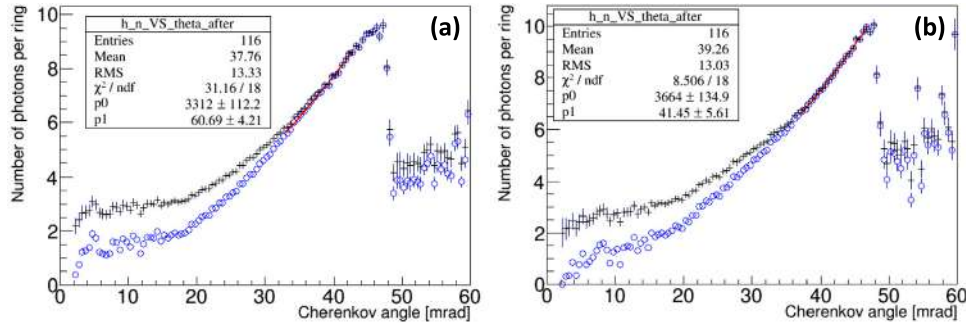


Fig. 32. Distribution of the mean number of photons per ring as a function of the Cherenkov angle, with (open circles) and without (crosses) applying the Poissonian correction, for two gaseous detectors: (a) a multiwire proportional chamber, (b) a micropattern gaseous detector. The Cherenkov angle does not reach the saturation value due to the momentum distribution of particles with Cherenkov images in the peripheral photon detectors. The decreasing distribution slope above the maximum is due to the finite resolution affecting the measured Cherenkov angle. The fit with function (1) is superimposed. The number of signal (background) photons, at saturation, are: 11.1 ± 0.2 (2.6 ± 0.2) and 12.0 ± 0.7 (1.6 ± 0.6) for the considered multiwire proportional chamber and micropattern gaseous detector, respectively.

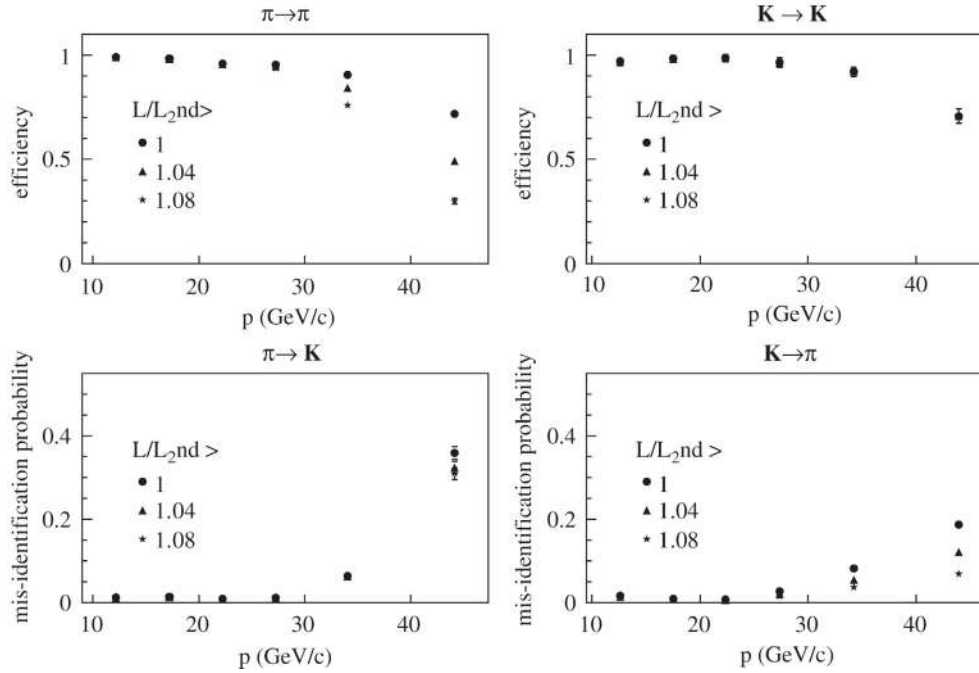


Fig. 33. Identification efficiency and mis-identification probability as a function of the particle momentum for different cuts applied to the ratio L/L_{2nd} ; pions and kaons from K_S and ϕ_{1020} decay, respectively [9].

charged pions and charged kaons) and in the whole COMPASS hadron spectroscopy programme.

A remarkable example of the RICH contribution to COMPASS physics results is provided in the identification of the open charm reaction by looking for D^0 production. The D mesons are selected through their decays in the two channels: $D^* \rightarrow D^0 \pi_{slow}^+ \rightarrow K^- \pi^+ \pi_{slow}^+$ (“ D^* sample”) and $D^0 \rightarrow K^- \pi^+$ (“ D^0 sample”), and their charge conjugates. In order to reduce the large combinatorial background, RICH-1 is used to identify the K and the π from the D^0 decay. For the identification of slow pions in the D^* channel, RICH-1 is used as a veto requiring the track not to be identified as an electron. For the D^* sample, the difference of the πK invariant mass and the D^0 mass is shown in Fig. 34, for data taken by the COMPASS Collaboration in 2006.

9. Conclusions

The RICH plays a key role in the COMPASS spectrometer and provided, over a period of 20 years, fundamental contributions to the scientific results by the experiment thanks to the careful design, the

continuous and rigorous maintenance and the several upgrade actions. It will remain one of the key components of the COMPASS spectrometer during the run scheduled in 2021. It is the backbone of hadron PID system in the future physics programme at the CERN SPS M2 beam line, anticipated in the letter of intent by the COMPASS++/AMBER collaboration [2].

Moreover, the RICH represents a collection of relevant technological achievements. It has contributed to establish gaseous photon detectors both in the original RD26 architecture based on multiwire proportional chambers with CsI photocathodes and in the novel approach based on micropattern gaseous detector-technologies, used for the first time in the RICH for single photon detection. In the optical sector, a number of original elements have been introduced to serve the large RICH mirror wall: the light mirror support structure, the joints connecting the mirrors to the structure and allowing for mirror alignment and the CLAM system, a fully optical system introduced to monitor the alignment of the mirror segments. The other RICH components, even if not original, represent the state-of-the-art: the radiator gas system and the setup for the measurement of the gas transparency in the UV range, the system to remove the pollutants from the radiator gas,

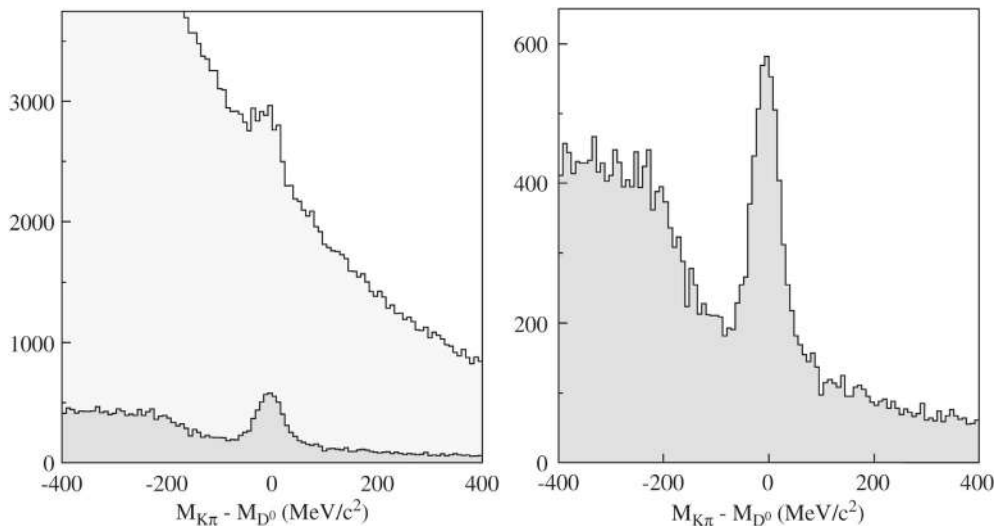


Fig. 34. Difference of the invariant mass and the D^0 mass, data taken in 2006 by the COMPASS Collaboration. Left: spectra without (light grey) and with (dark grey) PID. Right: zoom of the spectrum with PID [9].

the photon detector system based on multianode photomultiplier tubes coupled to individual fused silica lens telescopes, the mirrors with high reflectance in the UV range, the low noise electronic systems used to readout the gaseous photon detectors and the fine time resolution readout system for the multianode photomultiplier tubes. Thanks to all this, the COMPASS RICH contributes to consolidate and disseminate the technology of RICHes with gaseous radiator for hadron PID at high momentum, detectors highly need in flavour and hadron physics at high energies.

Declaration of competing interest

The authors declare that they have no known competing financial interests or personal relationships that could have appeared to influence the work reported in this paper.

Acknowledgements

COMPASS RICH could be designed, built, upgraded, operated and its data understood and analysed thanks to a large team, with variable composition over the 25 year-long life of the project. The detector could represent a technological success and could largely contribute to the COMPASS physics programme only thanks to the skill and dedication of all these colleagues.

A central role has been played by the INFN, Italy-University Trieste group dedicated to the COMPASS experiment, where Franco Bradamante, promoter of the COMPASS experiment, could obtain the financial support for the RICH, United States enterprise and gave to the author of this article the opportunity to coordinate the project, and where a number of colleagues have contributed with first-class professionalism and exceptional dedication. Among them, in particular: Stefano Levorato, Giorgio Menon, Paolo Schiavon and Fulvio Tassarotto.

The delicate enterprise of the UV mirror wall has been guided by Sergio Costa, from the INFN-University Torino group.

CERN colleagues from different divisions have provided irreplaceable contributions and it is a privilege to mention, in particular, Michel Bosteels, André Braem, Jean-Christophe Gayde, Olav Ullaland and Roger Valbuena. The guidance of Francois Piuz, CERN, has enormously helped in the starting approach to gaseous photon detectors.

The challenging design of the optical telescopes coupled to the multianode photomultiplier tubes could not be possible without Miroslav Sulc and his younger collaborators at the Technical University in Liberec.

The electronics designed by the colleagues of the ICTP-INFN Micro-processor Laboratory guided by Alberto Colavita has played a major role in the first phase of the RICH operation. The upgrade of the multiwire proportional chamber read-out has been realized by a TUM in Munich and IRFU-CEA at Saclay collaboration. The multianode photomultiplier tube read-out has been designed and realized by the COMPASS groups from the University of Freiburg and from INFN-University Torino.

Over years, central contributions have come from colleagues of various European Institutions in the COMPASS collaboration: the University of Bielefeld, the Charles University in Prague and, more recently, the University of Aveiro.

The author has found cultural support and precious suggestions in a number of friendly and fruitful conversations with Tom Ypsilantis. The series of international workshops dedicated to RICH detectors, that he initiated together with Eugenio Nappi (INFN-Bari), presently engaged in ensuring the continuity of the series, has represented a rich source of information and inspiration since the first one in Bari in 1993.

The micropattern gaseous detector-based photon detectors have been developed taking great advantage from the cultural environment, the know-how, the infrastructural support of the RD51 Collaboration, dedicated to the development and dissemination of micropattern gaseous detectors. The author expresses her gratitude to Eraldo Oliveri (CERN), Leszek Ropelewski (CERN) and Maxim Titov (CEA Saclay/Irfu) and to all the colleagues in the collaboration.

The author is grateful to all the colleagues of the COMPASS Collaboration, from whom continuous support and encouragement have come over the long life of the RICH project.

References

- [1] A complete list of the publications by the COMPASS Collaboration can be found in <https://greybook.cern.ch/greybook/experiment/detail?id=NA58>.
- [2] B. Adams, et al., The COMPASS++/AMBER Collaboration, Letter of Intent: A New QCD facility at the M2 beam line of the CERN SPS, CERN-SPSC-2019-003 (SPSC-I-250), [arXiv:1808.00848](https://arxiv.org/abs/1808.00848) [hep-ex].
- [3] P. Abbon, et al., The COMPASS Collaboration, The COMPASS experiment at CERN, *Nucl. Instrum. Methods A577* (2007) 455.
- [4] P. Abbon, et al., The COMPASS Collaboration, The COMPASS setup for physics with hadron beams, *Nucl. Instrum. Methods A779* (2015) 69.
- [5] E. Albrecht, et al., COMPASS RICH-1, *Nucl. Instrum. Methods A502* (2003) 112, COMPASS RICH-1; E. Albrecht, et al., First performances of COMPASS RICH-1, *Nucl. Instrum. Methods A518* (2004) 586.
- [6] E. Albrecht, et al., Status and characterisation of COMPASS RICH-1, *Nucl. Instrum. Methods A553* (2005) 215.

- [7] P. Abbon, et al., Design and construction of the fast photon detection system for COMPASS RICH-1, *Nucl. Instrum. Methods A*616 (2010) 21.
- [8] P. Abbon, et al., Read-out electronics for fast photon detection with COMPASS RICH-1, *Nucl. Instrum. Methods A*587 (2008) 371.
- [9] P. Abbon, et al., Particle identification with COMPASS RICH-1, *Nucl. Instrum. Methods A*631 (2011) 26.
- [10] E. Albrecht, et al., The radiator gas and the gas system of COMPASS RICH-1, *Nucl. Instrum. Methods A*502 (2003) 266.
- [11] E. Albrecht, et al., The mirror system of COMPASS RICH-1, *Nucl. Instrum. Methods A*502 (2003) 236.
- [12] G. Baum, et al., The COMPASS RICH-1 read-out system, *Nucl. Instrum. Methods A*502 (2003) 246.
- [13] P. Abbon, et al., A new analogue sampling readout system for the COMPASS RICH-1 detector, *Nucl. Instrum. Methods A*589 (2008) 362.
- [14] J. Agarwala, et al., The MPGD-based photon detectors for the upgrade of COMPASS RICH-1 and beyond, *Nucl. Instrum. Methods A*936 (2019) 416.
- [15] F. Tessarotto, et al., Long term experience and performance of COMPASS RICH-1, *JINST* 9 (2014) C09011.
- [16] The COMPASS Collaboration, Proposal, CERN/SPSLC/96-14, SPSC/p297, march 1, 1996, addendum, CERN/SPSLC/96-30, SPSLC/P297, Addendum 1, 1996.
- [17] E. Albrecht, et al., Performance of a prototype RICH detector using hybrid photodiodes, *Nucl. Instrum. Methods A*456 (2001) 190, private communication by E. Fokitis.
- [18] E. Albrecht, et al., VUV absorbing vapours in n-perfluorocarbons, *Nucl. Instrum. Methods A*510 (2003) 262.
- [19] M. Bosteels, Gases and liquids in RICH detectors, *Nucl. Instrum. Methods A*371 (1996) 248.
- [20] M.L. Andrieux, et al., Ultrasonic gas mixture analysis system in the forward RICH of DELPHI, *Nucl. Instrum. Methods A*371 (1996) 259.
- [21] P. Baillon, et al., A ring imaging cherenkov detector, the DELPHI Barrel RICH Prototype: Part A: Experimental studies of the detection efficiency and the spatial resolution, *Nucl. Instrum. Methods A*276 (1988) 492; P. Baillon, et al., A ring imaging cherenkov detector, the DELPHI barrel RICH prototype: Part B: Experimental studies of the detector performance for particle identification, *Nucl. Instrum. Methods A*277 (1988) 338.
- [22] S. Costa, et al., CLAM, a continuous line alignment and monitoring method, for RICH mirrors, *Nucl. Instrum. Methods A*533 (2005) 135.
- [23] M. Alexeev, et al., On-line mirror alignment monitoring method for COMPASS RICH-1, *Nucl. Instrum. Methods A*595 (2008) 194.
- [24] M. Alexeev, et al., Mirror alignment control for COMPASS RICH-1 detector, *Nucl. Instrum. Methods A*639 (2011) 219.
- [25] M. Alexeev, et al., Monitoring of absolute mirror alignment at COMPASS RICH-1 detector, *Nucl. Instrum. Methods A*766 (2014) 208.
- [26] T. Luhman, et al., Close Range Photogrammetry: Principles, Techniques and Applications, Whittles Publishing, Scotland, UK, 2006.
- [27] R & D26 collaboration, status reports: CERN/DRDC 93-36, 94-49, 96-20; The ALICE collaboration, Technical Design Report of the High Momentum Particle Identification Detector, CERN/ LHCC 98-19, ALICE TDR 1, 1998; F. Piuze, *Nucl. Instrum. Methods A*502 (2003) 692, 76.
- [28] A. Di Mauro, Recent CsI-RICH developments, *Nucl. Instrum. Methods A*525 (2004) 173.
- [29] H. Hoedlmoser, et al., Production technique and quality evaluation of CsI photocathodes for the ALICE/HMPID detector, *Nucl. Instrum. Methods A*566 (2006) 338.
- [30] C. Santiard, et al., Gassiplex: a low noise analog signal Processor for readout of gaseous detectors, Presented at the Sixth Pisa Meeting on Advanced Detector, La Biodola, Isola d'Elba, Italy, 1994.
- [31] M.J. French, et al., Design and results from the apv, a deep sub-micron CMOS front-end chip for the CMS tracker, *Nucl. Instrum. Methods A* 466 (2001) 359.
- [32] M. Alexeev, et al., Long term experience with CsI photocathodes in gas photon detectors, *JINST* 9 (2014) P01006.
- [33] W. Anderson, et al., Design, construction, operation and performance of a Hadron Blind Detector for the PHENIX experiment, *Nucl. Instrum. Methods A*646 (2011) 35.
- [34] M. Alexeev, et al., The quest for a third generation of gaseous photon detectors for Cherenkov imaging counters, *Nucl. Instrum. Methods A*610 (2009) 174; M. Alexeev, et al., THGEM based photon detector for Cherenkov imaging applications, *Nucl. Instrum. Methods A*617 (2010) 396; M. Alexeev, et al., Micropattern gaseous photon detectors for Cherenkov imaging counters, *Nucl. Instrum. Methods A*623 (2010) 129;
- M. Alexeev, et al., Development of THGEM-based photon detectors for Cherenkov imaging counters, *JINST* 5 (2010) P03009;
- M. Alexeev, et al., Progress towards a THGEM-based detector of single photons, *Nucl. Instrum. Methods A*639 (2011) 130;
- M. Alexeev, et al., Detection of single photons with ThickGEM-based counters, *JINST* 7 (2012) C02014;
- M. Alexeev, et al., Detection of single photons with ThickGEM-based counters, *Nucl. Instrum. Methods A*695 (2012) 159;
- M. Alexeev, et al., Development of THGEM-based photon detectors for COMPASS RICH-1, *Phys. Procedia* 37 (2012) 781;
- M. Alexeev, et al., THGEM-based photon detectors for the upgrade of COMPASS RICH-1, *Nucl. Instrum. Methods A*732 (2013) 264;
- M. Alexeev, et al., Ion backflow in thick GEM-based detectors of single photons, *JINST* 8 (2013) P01021;
- M. Alexeev, et al., Status and progress of novel photon detectors based on THGEM and hybrid MPGD architectures, *JINST* 8 (2013) C12005;
- M. Alexeev, et al., Progresses in the production of large-size THGEM boards, *JINST* 9 (2014) C03046;
- M. Alexeev, et al., MPGD-based counters of single photons developed for COMPASS RICH-1, *JINST* 9 (2014) C09017;
- M. Alexeev, et al., Status and progress of the novel photon detectors based on THGEM and hybrid MPGD architectures, *Nucl. Instrum. Methods A*766 (2014) 133;
- M. Alexeev, et al., MPGD-based counters of single photons for Cherenkov imaging counters, *PoS* (2014) 075;
- M. Alexeev, et al., The gain in Thick GEM multipliers and its time-evolution, *JINST* 10 (2015) P03026;
- M. Alexeev, et al., Status of the development of large area photon detectors based on THGEMs and hybrid MPGD architectures for Cherenkov imaging applications, *Nucl. Instrum. Methods A*824 (2016) 139.
- [35] L. Periale, et al., Detection of the primary scintillation light from dense Ar, Kr and Xe with novel photosensitive gaseous detectors, *Nucl. Instrum. Methods A*478 (2002) 377; P. Jeanneret, Time Projection Chambers and Detection of Neutrinos (Ph.D. thesis), Neuchatel University, 2001. P.S. Barbeau, et al., Toward coherent neutrino detection using low-background micropattern gas detectors, *IEEE NS- 50* (2003) 1285.
- R. Chechik, et al., Thick GEM-like hole multipliers: properties and possible applications, *Nucl. Instrum. Methods A*535 (2004) 303.
- [36] Y.Y. Giomataris, et al., MICROMEAS: a high-granularity position-sensitive gaseous detector for high particle-flux environments, *Nucl. Instrum. Methods A*376 (1996) 29.
- [37] I. Giomataris, et al., Micromegas in a bulk, *Nucl. Instrum. Methods A*560 (2006) 405.
- [38] S.S. Dasgupta, Particle Identification with the Cherenkov Imaging Technique using MPGD Based Photon Detectors for Physics at COMPASS Experiment at CERN (Ph.D. thesis), University of Trieste, 2017.
- [39] F. Paschen, Über die zum Funkenübergang in Luft, Wasserstoff und Kohlensäure bei verschiedenen Drucken erforderliche Potentialdifferenz, *Ann. Phys.* 273 (1889) 69.
- [40] J. Agarwala, et al., The high voltage system with pressure and temperature corrections for the novel MPGD-based photon detectors of COMPASS RICH-1, *Nucl. Instrum. Methods A*942 (2019) <http://dx.doi.org/10.1016/j.nima.2019.162378>.
- [41] S. Korpar, et al., The HERA-B RICH, *Nucl. Instrum. Methods A*433 (1999) 128.
- [42] HAMAMATSU, Multianode Photomultiplier tube assembly H8711, Technical Data.
- [43] M. Chiosso, et al., A fast binary front-end ASIC for the RICH detector of the COMPASS experiment at CERN, in: 2008 IEEE Nuclear Science Symposium Conference Record, N11-4, 2008.
- [44] H. Fischer, et al., Implementation of the dead-time free FI TDC in the COMPASS read-out, *Nucl. Instrum. Methods A*461 (2001) 506.
- [45] J. Hartmann, Bemerkungen über den Bau und die Justirung von Spektrographen, *Zt. Instrum.* 20 (1900) 47.
- [46] G. Baum, et al., RICHONE: a software package for the analysis of COMPASS RICH-1 data, *Nucl. Instrum. Methods A*502 (2003) 315.
- [47] R.J. Barlow, Extended maximum likelihood, *Nucl. Instrum. Methods A*297 (1990) 496.
- [48] R. Forty, RICH pattern recognition for LHCb, *Nucl. Instrum. Methods A*433 (1999) 257.
- [49] M. Starič, P. Krizan, An iterative method for the analysis of cherenkov rings in the HERA-B RICH, *Nucl. Instrum. Methods A*433 (1999) 279.